High resolution imaging polarimetry of HL Tau and magnetic field structure*

P.W.Lucas[1], Misato Fukagawa[2], Motohide Tamura[3], A.F.Beckford[1],
Yoichi Itoh[4], Koji Murakawa[5], Hiroshi Suto[5], Saeko S. Hayashi[5],
Yumiko Oasa[4], Takahiro Naoi[6], Yoshiyuki Doi[5], Noboru Ebizuka[7],
and Norio Kaifu[3]

* *Based in part on data collected at Subaru Telescope, which is operated by the National Astronomical Observatory of Japan.*
[1] *Dept. of Physical Sciences, University of Hertfordshire, College Lane, Hatfield AL10 9AB, UK*
 email: pwl@star.herts.ac.uk
[2] *Dept. of Astronomy, University of Tokyo, 7-3-1 Hongo, Bunkyo, Tokyo 113-0033, Japan*
[3] *National Astronomical Observatory of Japan, 2-21-1, Osawa, Mitaka, Tokyo 181-8588, Japan*
[4] *Graduate School of Science and Technology, Kobe University, 1-1 Rokkodai, Nada, Kobe 657-8501, Japan*
[5] *Subaru Telescope, 650 North A'ohoku Place, Hilo, HI 96720, USA*
[6] *Dept. of Earth and Planetary Science, University of Tokyo, 7-3-1 Hongo, Bunkyo, Tokyo 113-0033, Japan*
[7] *The Institute of Physical and Chemical Research, 2-21 Hirosawa, Wako, Saitama 351-0198, Japan*

ABSTRACT
We present high quality near infrared imaging polarimetry of HL Tau at 0.4 to 0.6
arcsec resolution, obtained with Subaru/CIAO and UKIRT/IRCAM. 3-D Monte Carlo
modelling with aligned oblate grains is used to probe the structure of the circumstellar
envelope and the magnetic field, as well as the dust properties. At J band the source
shows a centrosymmetric pattern dominated by scattered light. In the H and K bands
the central source becomes visible and its polarisation appears to be dominated by
dichroic extinction, with a position angle inclined by $\approx 40°$ to the disc axis. The
polarisation pattern of the environs on scales up to 200 AU is consistent with the same
dichroic extinction signature superimposed on the centrosymmetric scattering pattern.
These data can be modelled with a magnetic field which is twisted on scales from tens
to hundreds of AU, or alternatively by a field which is globally misaligned with the
disc axis. A unique solution to the field structure will require spatially resolved circular
polarisation data. The best fit Monte Carlo model indicates a shallow near infrared
extinction law. When combined with the observed high polarisation and non-negligible
albedo these constraints can be fitted with a grain model involving dirty water ice
mantles in which the largest particles have radii slightly in excess of 1 μm. The best
fit model has an envelope structure which is slightly flattened on scales up to several
hundred AU. Both lobes of the bipolar outflow cavity contain a substantial optical
depth of dust (not just within the cavity walls). Curved, approximately parabolic,
cavity walls fit the data better than a conical cavity. The small inner accretion disc
observed at millimetre wavelengths is not seen at this spatial resolution.

Key words: polarization - (stars:) circumstellar matter - (stars:) individual: HL Tau

1 INTRODUCTION

HL Tau is among the most well studied of all Young Stellar
Objects (YSOs). It is a low mass YSO in the nearby Taurus-
Auriga star formation region with a spectral energy distribu-
tion which is Class I but relatively flat between wavelengths
2 to 60 μm (Men'shchikov, Henning & Fischer 1999). This
indicates an evolutionary status fairly close to the bound-

ary between Class I and Class II YSOs, sometimes known
as flat spectrum T Tauri stars (Adams, Lada & Shu 1988).
Such sources are astrophysically very useful. They often re-
tain a large circumstellar envelope, which can provide clues
to the formation process, but the optical depth of the enve-
lope is low enough that the central regions can be observed
in the near infrared waveband with high spatial resolution
and high signal to noise ratio. The system is surrounded

by an unusually massive envelope ($\sim$ 0.1 M$_\odot$, Beckwith et al. 1986; 1990) with a radius of approximately 1300 AU. It has been claimed that this structure is rotating (Sargent & Beckwith 1991) or infalling (Hayashi et al. 1993) but later work (Cabrit et al. 1996) casts doubt on these suggestions and indicates that the kinematics are complicated by the entrained outflow. Recent ^{13}CO mapping of the large scale environment (Welch et al. 2000) finds that the kinematics are further confused by the presence of an expanding shell around the adjacent T Tauri star XZ Tau, which has recently reached the location of HL Tau.

Close et al.(1997) imaged HL Tau at 0.2 to 0.3 arcsec resolution with adaptive optics (AO). They observed a compact irregular nebula containing a point source which was bright in the H (1.65 μm) and K (2.2 μm) bands but less prominent in the J band (1.25 μm) where the extinction is higher. Optical imaging at even higher spatial resolution with HST (Stapelfeldt et al. 1995) showed only circumstellar nebulosity and no point source, demonstrating the embedded nature of the system.

Imaging provides only limited information on the structure of a YSO nebula the dust grains within it. This is particularly true in systems like HL Tau where the central source is so bright at 2 μm that details of the circumstellar matter are lost in the skirts of the image profile. Imaging polarimetry circumvents this latter problem (the central source being much fainter in polarised light) and provides a wealth of additional information on the nature of circumstellar dust grains and the physical structure of the envelope (eg. Tamura et al.1991; Whitney & Hartmann 1993; Fischer, Henning & Yorke 1994; 1996; Gledhill et al. 1996; Lucas & Roche 1997, 1998 (hereafter LR97, LR98); Whitney et al. 1997). Polarimetry can also yield information on the magnetic field structure within the circumstellar envelope, since non-spherical dust grains in the protostellar environment are believed to rapidly align their axis of greatest rotational inertia so that it precesses around the axis of the local magnetic field. Note that the degree of grain alignment and the dominant alignment mechanism remain uncertain (radiative torque alignment or paramagnetic alignment aided by H$_2$ rotation torques; see recent review by Lazarian 2003) but it is reasonably certain that the sense of the grain precession axis is parallel to the magnetic field direction (Draine & Weingartner 1997).

Near infrared polarimetry of point source Class II and Class III YSOs usually reveals only a low degree of polarisation due to dichroic extinction by aligned grains. Polarimetry of Class I YSOs with circumstellar nebulae often shows a region of aligned vectors known as a 'polarisation disc' at the location of the central source, and a gradual transition to a centrosymmetric pattern of vectors in the surrounding nebula. These polarisation discs are often attributed to multiple scattering in cases where the optical depth toward the central source is too high for direct observation (Whitney et al.1993; Bastien & Menard 1988). However, polarisation discs are also sometimes observed in cases where the optical depth is low (eg. TMR-1, see LR97) and the multiple scattering mechanism does not easily reproduce the high polarisation ($>$ 15%) of the polarisation disc seen toward some sources (eg. IRAS 04302+2247, see LR97). Alternative mechanisms must therefore be considered also, including: (1) scattering and extinction by aligned non-spherical

grains (Gledhill & McCall 2000; Whitney & Wolff 2002; Lucas 2003; Lucas et al. 2003); and (2) artifacts of the seeing profile, which we call the 'illusory disc' (see Whitney et al.1997 and LR98).

HL Tau was therefore identified as an ideal subject for imaging polarimetry at high spatial resolution in the JHK bands, since at the 0.4 arcsec resolution commonly achieved in good seeing conditions at Mauna Kea Observatory (without Adaptive Optics) it was anticipated that the central source would be obscured by nebulosity at J band, but become visible in the H and K bands. This proved to be the case, as previously found by Beckwith & Birk (1995) in 1 arcsec resolution data. The data collection is described in section 2, the observational results are described in section 3, and sections 4 and 5 detail the methodology and results of 3-D Monte Carlo modelling of the system with aigned grains. The conclusions are listed in section 6.

2   OBSERVATIONS

Near infrared imaging polarimetry was independently carried out with 2 telescopes at Mauna Kea Observatory on dates a few weeks apart, providing a useful test of the reliability of the data. The 3.8-m United Kingdom Infrared Telescope (UKIRT) was used on 28th December 2000 by observatory staff as part of the UKIRT Service programme, using flexible scheduling to ensure good seeing conditions. Observations were made in the J, H and K bands with the camera IRCAM. The 8.2-m Subaru Telescope was used on 17th January 2001 during commissioning of the Coronographic Imager with Adaptive Optics (CIAO, see Tamura et al. 2000). The Subaru observations were conducted in H and K bands, but the high quality data was obtained only in the K band. The H band data was taken at high airmass ($\gtrsim$ 1.8) and with less integration time and suffered from imperfect tracking which obscured small scale structures. We will not discuss the Subaru H band data quantitatively. Although the Subaru AO system was not used, good seeing conditions allowed 0.4 arcsec resolution to be obtained (full-width half maximum). Both datasets were taken in photometric conditions. The UKIRT dataset suffered from an offset from correct focus which slightly reduced the spatial resolution and data quality (see below). However the spatial resolution was still 0.4 to 0.6 arcsec and the focus tracking system provided excellent image stability, which is indicated by both the consistency of subsets of the polarisation measurements in small apertures (see Section 3.2) and the good agreement between the Subaru and UKIRT datasets.

2.1   Subaru data

The Subaru/CIAO observations were conducted with a single beam system, using a cold wire grid analyser. A half wave plate modulator is placed upstream of any optical components except telescope optics including adaptive optics system, which minimizes the effect of AO mirrors on instrumental polarisation (IP), resulting in IP$<$ 1%. The image scale on the 1024^2 InSb ALADDIN II array was 0.022 arcsec pixel^{-1}. The warm modulator was rotated in sequence through position angles 0°, 22°.5, 45°, 67°.5 to measure the Stokes I, Q and U parameters. HL Tau was

observed with read noise limited integrations of 1 s, and 10 exposures were coadded into one image frame. Before rotating the modulator, 6 image frames were taken (i.e. 60 s of data). The integration time per modulator cycle was 240 s (4 modulator positions) and 4 consecutive modulator cycles were performed at different dither positions on the array. The total on source integration time at K band was 960 s. A polarised star HD251204 (Weitenbeck 1999) was observed following HL Tau, providing a reliable determination of the position angle calibration. Several other standards taken at the later commissionings of the CIAO polarimeter gave consistent values for the position angle calibration. The polarisation efficiency was measured with an unpolarized star and another wire grid analyser inserted over the half wave plate, making 100% polarisation artificially. The efficiency of 97% in K band was applied for the calibration of observed polarisation degree. Individual frames were calibrated in the usual manner with the reduction packages in IRAF: dark subtraction, flat-fielding by dome-flats, bad-pixel substitution, and sky subtraction. Since there is no difference between flats taken at four modulator angles, all flats were combined and used in order to obtain higher signal-to-noise. The dithered frames taken just before and after the calibrated frame were combined to use as a sky frame for background subtraction.

2.2 UKIRT data

The UKIRT/IRCAM observations were conducted with a dual beam system with a cold Wollaston prism inside IR-CAM and a half waveplate modulator mounted in IRPOL-2 (see Hough et al., 1995). Dual beam systems reduce the effect of variations in seeing and transparency between different rotation settings of the modulator. The warm modulator was rotated in the same sequence as Subaru. The image scale on the 256^2 InSb array was 0.08 arcsec pixel^{-1}, following the reconfiguration of the camera as IRCAM-TUFTI in early 1999. A warm mask mounted on the camera entrance window prevents overlap of the dual beams, and divides the useful observing area on the sky into 2 parallel strips 20 arcsec in length and 4 arcsec wide. HL Tau was observed in 10 s observation blocks at each waveplate position before rotating the modulator or dithering the target position, in order to smooth out the effect of any short term variations in the image profile. The total coadded exposure time was 240 s at J band, 240 s at H band and 360 s at K band but individual exposures were short and read noise limited, due to the brightness of the target. No polarisation standards were observed with UKIRT but observatory staff have found the IRPOL-2 system to be stable over many years, with polarisation efficiency > 99% and a consistent position angle calibration relative to north ($6.7 \pm 0.1°$). Note that IRPOL2 lies above IRCAM in the light path, so the camera affects the measured polarisaton only through (i) the efficiency of the Wollaston in IRCAM (> 99%); and (ii) a rotation of the image plane with respect to north which must be reversed in order to match the image data to the polarisation data. The image rotation is $-88.84 \pm 0.08°$, see www.jach.hawaii.edu/JACpublic/UKIRT/home.html. The UKIRT data were dark subtracted and flatfielded in IRAF before commencing polarimetric reduction using the Star-

link package POLPACK. Individual frames were registered using the central flux peak of HL Tau, which is very well defined in the H and K bands, permitting precision of a small fraction of a pixel. The J band registration using the more nebulous flux peak was less precise but still accurate to 1 pixel or better (0.08 arcsec).
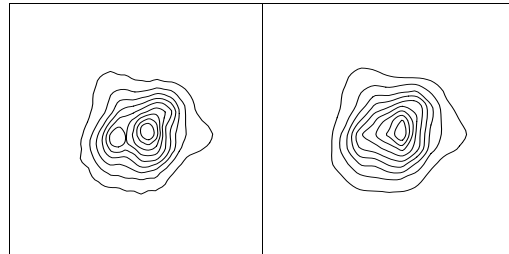

Figure 1. UKIRT image profile from 27 December 2000. (left) as observed. (right) after rebinning to the 0.15 arcsec pixel scale used in the models in Section 5. Contour levels are 0.1, 0.2, 0.3 ... 0.9, normalised to unity at the peak.

Focussing Problem

The focus offset mentioned above caused the UKIRT K band data to show a small secondary peak on the shoulder of the image profile (see Figure 1) located 0.4 arcsec from the principal peak at P.A.=103° (east of north) and with $\sim 90\%$ of the peak intensity. Inspection of K band archival imaging data of an isolated star taken on the previous night (27 December) clearly shows the secondary source appearing at the same location as the focus was changed in a sequence from in focus to far out of focus. This introduced the spurious secondary source in the HL Tau K band data, which shows the same percentage and position angle of polarisation as the main peak. The secondary source had $\sim 70\%$ of the peak intensity in the profile of the isolated star but appears at a higher level in the HL Tau data due to the bright underlying nebulosity. Additional archival imaging polarimetry taken 2 weeks later in very good seeing conditions (0.3 to 0.4 arcsec) shows that there is no sign of this secondary source when the telescope is well focussed, confirming that the artefact was not caused by the Wollaston prism or the IRPOL-2 waveplates.

Despite the focus offset the UKIRT tip/tilt secondary mirror and focus tracking system ensured that the image profile was very stable, with no variation being detectable between the 36 individual K band frames or the J and H band frames. This is confirmed by the consistent results of small aperture polarimetry in independent cycles of the modulator (see section 3.2). The effect of the problem is therefore simply to reduce the spatial resolution of the data slightly to approximately 0.55 arcsec (see end of section 4).

3-micron Spectrum

An L band spectrum of HL Tau was taken with UKIRT

and the near infrared spectrograph CGS4 on 1st December 1998. These data were also taken in Service mode by observatory staff. The data were obtained in order to search for the 'Unidentified Infrared Bands' sometimes seen in more massive YSOs, which are often attributed (Sellgren 1984) to UV excited emission by ionised polycyclic aromatic hydocarbons (PAHs). A 40 l/mm grating was used, giving a spectral resolution of R=1320 and a wavelength span of 3.0 to 3.62 μm. While no PAH emission was detected, the strong water ice absorption seen in the spectrum is relevant to the discussion of grain composition in Section 5.2.3.

3   RESULTS

Polarisation maps and polarised flux images in the K, H and J bands are shown in Figures 2(a-d), 3(a-c) and 4(a-b). More detailed K and H band polarisation maps of the central regions are shown in Figure 5(a-c). The structure of the HL Tau nebula is indicated by contours overlaid on the polarisation maps. The flux distribution is dominated by a point source in the K and H bands but this suffers sufficient extinction within the system that circumstellar nebulosity is easily visible at the 0.4 arcsec resolution of the data. At J band the optical depth is sufficient to obscure the point source at this spatial resolution. The J band flux peak is dominated by scattered light and is offset from the centre of the polarisation pattern by 0.40 ± 0.11 arcsec along the disc axis. (We define the centre of the pattern using the polarisation nulls seen to either side of the region of low polarisation located southwest of the flux peak in Figure 4(a).) This contrasts with the observations of Close et al.(1997), wherein the higher spatial resolution (0.3 arcsec) reduced the nebulous flux in the beam by a factor of ~ 2 relative to these data, so that the point source was marginally detectable. Close et al. subracted a model of the nebulosity based on Hubble Space Telescope I band data (Stapelfeldt et al. 1995) to reveal the point source more clearly. The polarisation of the J band flux peak in our data is rotated by $\sim 50°$ compared to the position angle seen at H and K and has an approximately centrosymmetric orientation (see section 3.2), confirming that we observe a scattering peak at J band.

The UKIRT K band data show the small secondary flux peak 0.4 arcsec east of the central point source which is the image artefact caused by the focussing offset described in Section 2.2. The H and J band data also show an easterly elongation of the contours within 0.4 arcsec of the surface brightness peaks in Figures 3(a) and 4(a) but the false secondary peak is not resolved since the surface distributions are too smooth at these wavelengths.

The central point source is located at the approximate focus of the centrosymmetric pattern of polarisation vectors in the surrounding nebula. In the Close et al.(1997) data its spatial location is the same at J, H and K to within 0.1 arcsec so it is therefore simply interpreted as the protostar itself. In later sections of this paper the term 'protostar' is used synonymously with the central point source which is observed here only at H and K. Most (but not all) other researchers have made the same interpretation after observing the near concidence of both the millimetre source and the centimetre source with the infrared source (see Mundy et al.1996; Wilner, Ho & Rodriguez 1996; Rodriguez et al.1992; 1994). This is further supported by the presence of the optical jet extending away from this location (Mundt et al. 1990; Bacciotti, Eisloffel & Ray 1999).

Lower resolution infrared polarisation maps of the object have been made by Yamashita, Hodapp & Moore (1994); Weintraub, Kastner & Whitney (1995); Takami et al.(1999); Bastien et al.(private comm.). LR98 published Shift and Add polarimetry of HL Tau in the H and L bands at similar spatial resolution to these data but with much lower signal to noise. The optical polarisation structure has been mapped by Gledhill & Scarrott (1989). These previous lower resolution polarisation maps show the same centrosymmetric structure as observed here but did not resolve the distinct position angle of polarisation of the central point source, seen in the UKIRT and Subaru data (see section 3.3). The dense accretion disc indicated by the dark lane seen in polarised flux in Figure 2(d) was also observed with the same orientation by Yamashita et al.(1994). Weintraub et al.(1995) and LR98 also deduced this disc orientation from the region of low polarisation seen in the polarisation maps between the two highly polarised outflow lobes.

Weintraub et al.(1995) argued that the central flux peak is not in fact the protostar and that it is dominated by scattered light even in 0.4 arcsec resolution observations such as the speckle data of Beckwith et al.(1989). This was motivated partly by the apparent offset of the K band flux peak from the focus of the centrosymmetric vectors. (The focus is not a unique position since the centrosymmetry is imperfect but Weintraub et al. were able to determine a best average focus location). However, this offset may simply be due to the much lower spatial resolution of the Weintraub et al.(1995) measurement (using a camera with a 0.73 arcsec pixel scale), which might well have caused the flux peak to be dominated by scattered light. In addition, Monte Carlo modelling shows that the focus of the centrosymmetric vectors is unlikely to be coincident with the protostar in systems where the disc axis is inclined to the plane of the sky, (see LR98 and comment by Weintraub et al. 1995). In view of the later 0.2 arcsec resolution observations of Close et al.(1997) and the L band data of LR98 (which showed a very bright, essentially unpolarised point source at 0.2 arcsec resolution and little nebulosity) we therefore argue that the protostar is observed directly in high resolution near infrared observations, with the precise wavelength depending on the spatial resolution. Spectropolarimetry by Kobayshi et al.(1999) from 0.9 to 4.2 μm showed a steep decline in polarisation with wavelength (using large apertures) which also suggests the emergence of a point source.

A component of emission from hot dust very close to the protostar may also contribute to the central point source. Close et al. estimated from the weakness of NaI absorption at 2.21 μm that hot dust from the (spatially unresolved) innermost part of the accretion disc contributes 75% of the point source flux at K band, veiling the infrared spectrum observed by Greene & Lada (1996). However this does not take into account the low surface gravity of protostellar atmospheres, relative to field dwarfs of similar spectral type (type K). Sources with low gravity have weaker NaI absorption in the optical and the infrared (eg. Luhman et al.1998; Lucas et al. 2001) so the contribution from hot dust may be much less than 75%, though it is hard to quantify.
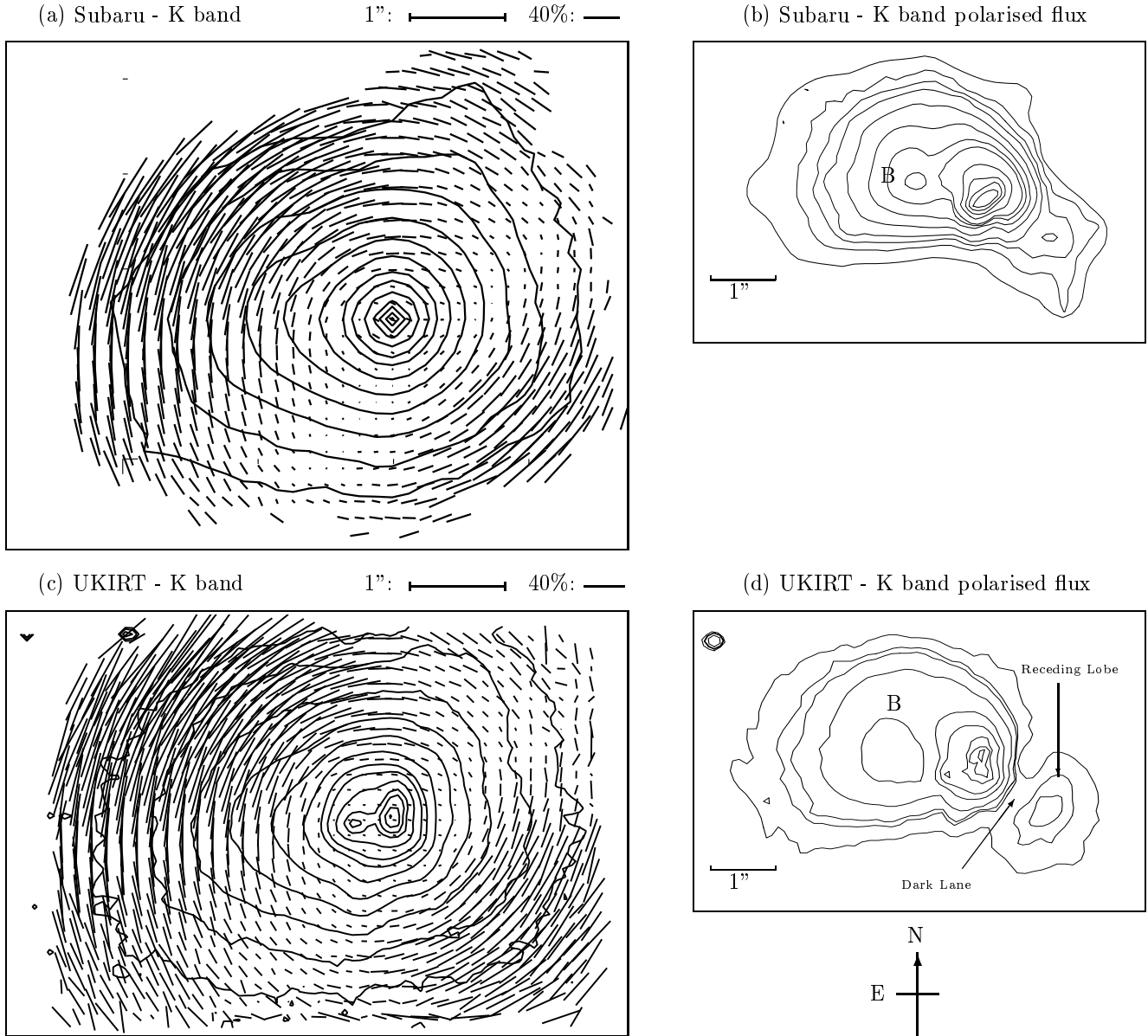
(a) Subaru - K band   1": ⊢────⊣   40%: ▬

(b) Subaru - K band polarised flux

(c) UKIRT - K band   1": ⊢────⊣   40%: ▬

(d) UKIRT - K band polarised flux

Figure 2. K band data. (a) Subaru image and polarsation map; (b) Subaru polarised flux image; (c) UKIRT image and polarisation map; (d) UKIRT polarised flux map. The data from both telescopes are very similar. The receding lobe of the bipolar nebula appears at lower contrast in the Subaru polarised flux data than the UKIRT data because the central peak is more highly polarised and better resolved in the Subaru data (see Table 1). The polarisation vectors are 8×8 binned in (a) and 2×2 binned in (c), giving pixel scales of 0.17 arcsec and 0.16 arcsec for the Subaru and UKIRT data respectively. Contour levels are normalised to unity at the peak. The levels in (a) and (c) are: 0.0031, 0.0063, 0.0125, 0.025, 0.05, 0.1, 0.2, 0.3, 0.5, 0.7, 0.8, 0.9, 0.99. Contour levels in (b) are 0.028, 0.05, 0.061, 0.1, 0.2, 0.3, 0.5, 0.7, 0.9. Levels in (d) are 0.019, 0.029, 0.039, 0.049, 0.07, 0.1, 0.137, 0.174, 0.3, 0.5, 0.7, 0.9, with the lowest contour level averaged using 2×2 pixel binning.

3.1 Polarised flux data

The structure of the system cannot easily be inferred from the irregular nebulosity of the total flux images (Figure 2(a,c), Figure 3(a) and Figure 4(a)). However, the polarised flux data (Figure 2(b,d), Figure 3(b,c), Figure 4(b)) suppresses the weakly polarised point source and reveals the receding lobe of the circumstellar envelope to the southwest and a dark lane of dense matter in between. The orientation of the plane of the disc and envelope inferred from the dark lane is $136° \pm 8°$ (east of north) and is broadly consistent with the value of $125° \pm 10°$ derived from millimetre data, see Section 5.1. The receding lobe is quite prominent and well defined in at K band, still more prominent at H band, but quite faint and diffuse at J band. This strong wavelength dependence, combined with the offset of the peak in total flux at J band, is a powerful constraint on the envelope's vertical density gradient and the extinction law, as shown in section

(a) UKIRT - H band

(a) UKIRT - J band

(b) UKIRT - H band polarised flux

(b) UKIRT - J band polarised flux

(c) Subaru - H band polarised flux
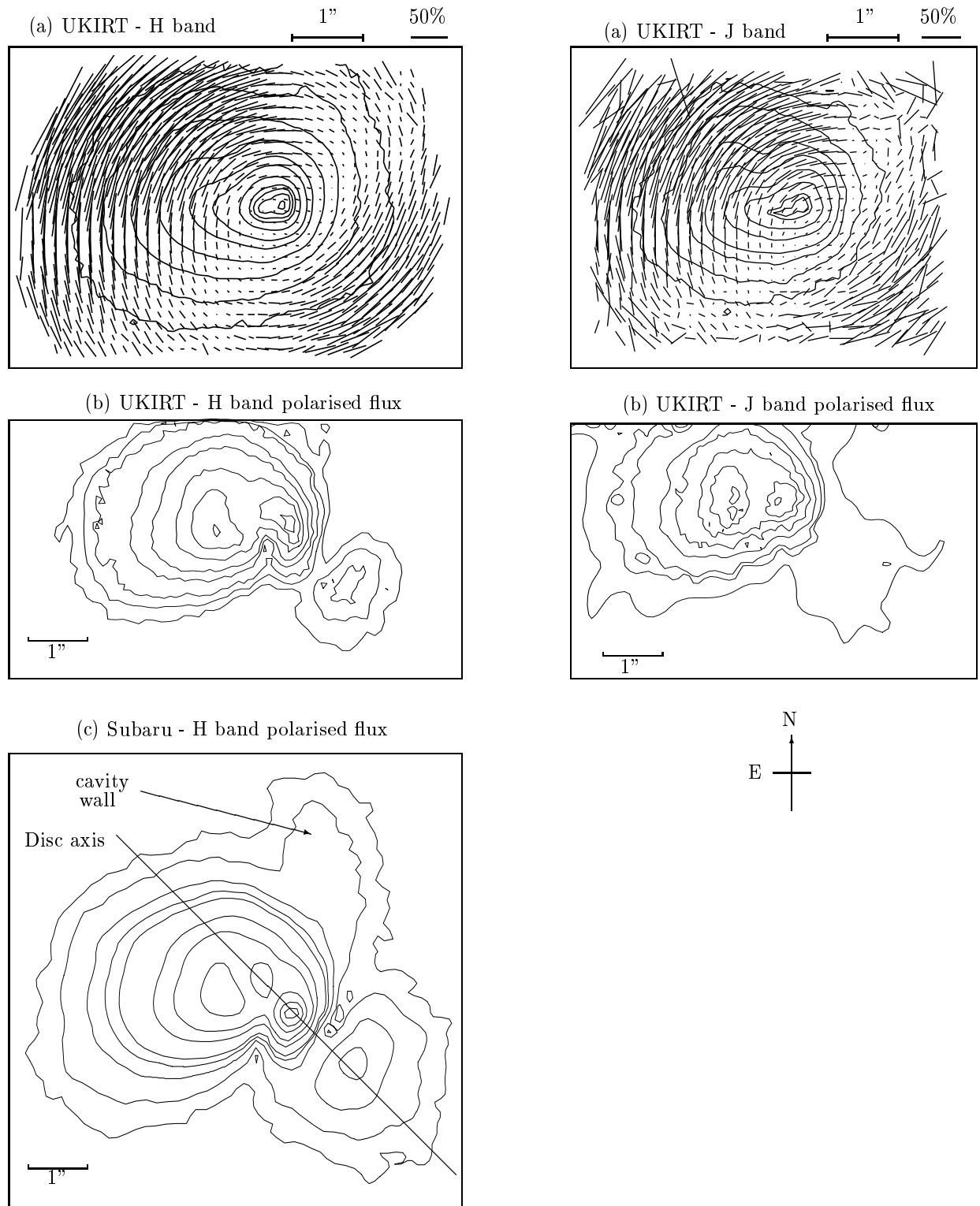
cavity
wall

Disc axis

N

E

Figure 3. H band data (left panels). (a) UKIRT image and polarisation map; (b) UKIRT polarised flux image; (c) Subaru polarised flux image, covering a larger field of view. The UKIRT polarisation vectors are 2×2 binned as in Figure 2. Contour levels are normalised to unity at the peak. The levels in (a) are: 0.0125, 0.025, 0.05, 0.1, 0.2, 0.3, 0.5, 0.7, 0.8, 0.9, 0.98. Contour levels in (b) are 0.05(2), 0.075(2), 0.1, 0.2, 0.3, 0.5, 0.7, 0.9, where the '(2)' indicates contouring of 2×2 binned pixels. Levels in (c) 0.015, 0.025, 0.05, 0.075, 0.1, 0.2, 0.3, 0.5, 0.7, 0.9.

Figure 4. J band data (right panels). (a) UKIRT image and polarisation map; (b) UKIRT polarised flux image. The UKIRT polarisation vectors are 2×2 binned as in Figure 2. Contour levels are normalised to unity at the peak. The levels in (a) are: 0.05, 0.1, 0.2, 0.3, 0.5, 0.7, 0.9, 0.95. Levels in (b) are 0.039(4), 0.07(2), 0.1(2), 0.2(2), 0.3, 0.5, 0.7, 0.9, where the '(n)' indicates contouring of n×n binned pixels.

5. The receding lobe appears less prominent in the Subaru K band polarised flux data than the UKIRT data only because the central point source is more highly polarised in the Subaru data (see section 3.2), so that the receding lobe and the dark lane appear at lower contrast. The polarisation of the receding lobe is the same in both datasets, and increases rapidly with distance from the protostar.

Other noteworthy features of the polarised flux data are:

(i) a broad peak (Source B) in the nebulosity located 1.3 arcsec east of the protostar, interpreted as asymmetrically distributed matter within the approaching lobe of the outflow cavity (see section 5)

(ii) a curved filament of nebulosity extending north from the vicinity of the protostar, seen in Figure 3(c). The filament is also seen in more recent non-polarimetic Subaru imaging data taken with AO (Tamura et al. 2004), and the outer part of it was seen in some previous imaging (Close et al. 1997; Takami et al. 1999). The filament is interpreted as the northern limb of the cavity wall associated with the approaching lobe of nebulosity. The eastern limb is not seen because it is obscured by the bright dust in the cavity observed as Source B (see models in Section 5).

A non axisymmetric distribution of cavity dust is not particularly surprising since the orientation of the jet and outflow shows signs of varying over time (Close et al.; Mundt et al). Moreover, Welch et al.(2003) report the detection of a companion millimetre continuum source with significant mass ($M > 10^{-3}$ M$_\odot$) at P.A.$\approx 315°$ some 0.6 arcsec (84 AU) from the centre of main accretion disc (radius 0.45 arcsec or 63 AU). The nature of the companion source is unclear (a dust cloud or a binary companion are both possible) but it may well influence the structure of the outflow cavity. The millimetre companion is not seen in the IR.

3.2 Polarisation maps and magnetic field structure

The most interesting feature of the polarisation maps is that the polarisation vectors associated with the protostar are inclined by between $30°$ and $45°$ to the disc plane. The 0.16-0.17 arcsec pixel scales used in Figures 2, 3 and 4 oversample the spatial resolution so several polarisation vectors around the protostar with very similar orientation are seen in the Subaru and UKIRT K band polarisation maps and the UKIRT H band map (the Subaru H band vector map suffered from imperfect tracking, which obscured small scale structures and is therefore not shown). Figure 5(a-c) shows a more detailed view of the central regions, with the UKIRT data unbinned (0.081 arcsec pixels) and the Subaru data 4 × 4 binned (0.088 arcsec pixels).
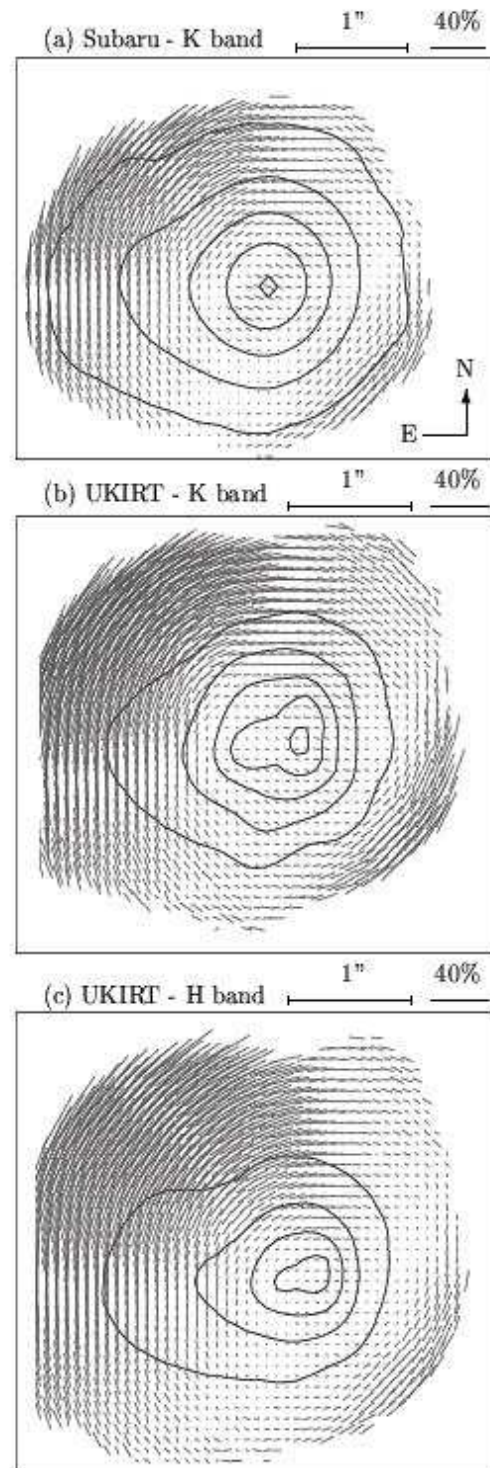

Figure 5(a-c). The central region in close up. (a) Subaru K band data (4 × 4 binned) to a 0.088 arcsec pixel scale. (b) UKIRT K band data. (c) UKIRT H band data. UKIRT data are unbinned, giving a 0.081 arcsec pixel scale. The vectors asscoiated with the central source appear somewhat inclined to the disc axis. The orientation of the disc axis can be inferred from bipolar structure of the vector pattern in each plot, although the true disc orientation measured at millimetre wavelengths is a little different (see text).
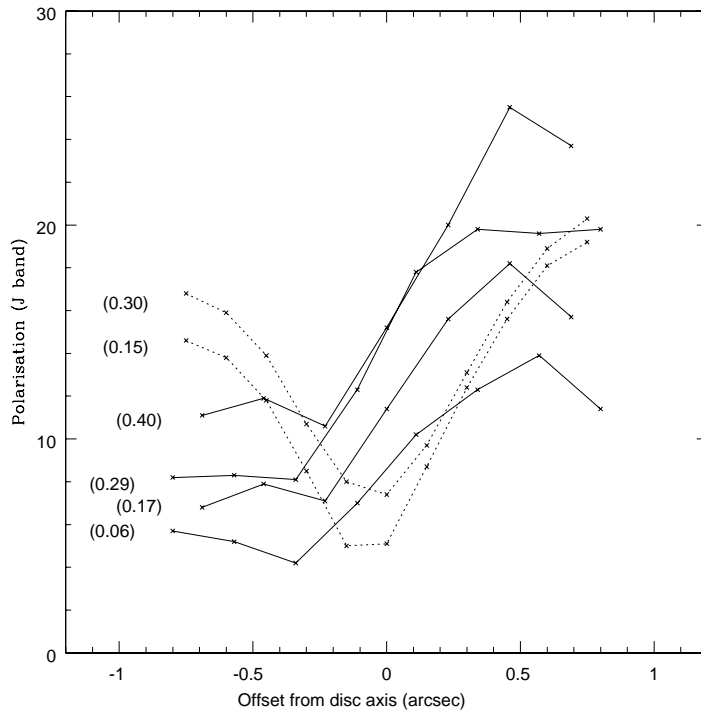
Figure 6. Asymmetry of J band polarisation. The plot shows several cuts across the disc axis in the approaching lobe: solid lines are data, dotted lines are model results. The location of each cut in arcseconds north east of the J band flux peak is marked. Polarisation in both the models and the data is higher to the right of the axis (positive offsets) and increases with distance along the axis. The polarisation gradient across the axis in the models is due to dichroic extinction of scattered light (see text). The effect in the data is greater and more spatially extended than in the models, suggesting that additional factors may be at work, eg. the structural asymmetry of the nebula. A P.A. of 45° is adopted for the disc axis in this plot to avoid rotating and resampling the data but this P.A. has some uncertainty (see text). Cuts using a P.A. of 35° (not shown) agree better with the rise in polarisation at negative offsets seen in the models but show a declining polarisation at $X > 1$ arcsec.

The small group of inclined vectors associated with the central source is easily fitted using the unresolved protostar in the models in section 5. The position angle and degree of polarisation observed by UKIRT and Subaru around the protostar are a little different (see Table 1) but the structure is qualitatively the same in both datasets and the difference is probably due to measurement error. The uncertainties in the polarisation measurements for the small aperture used in Table 1 are likely to be dominated by changes in the image profile between waveplate positions rather than photon shot noise or registration error. The models described in section 5 show that the measured polarisation at K band in a 0.4 arcsec aperture is insensitive, to first order, to the slight difference in spatial resolution of the two datasets. The uncertainties in Table 1 are estimated from internal variations of the measurements in subsets of the data: UKIRT had 3 independent cycles of the waveplate position and Subaru had 4 independent cycles. The individual UKIRT K band cycles had values of 3.39%, 3.35% and 3.86% for the central source. These average to a slightly lower value due to slightly different position angles in each subset. The UKIRT data has higher precision than Subaru due to the dual beam system of IRCAM. In theory the stable focus offset should not affect the measurement. However it is possible that the Subaru measurement is in fact more accurate because of the

UKIRT focussing problem so both datasets were taken into account when deriving uncertainties in model parameters.

The typical polarisation in both lobes of the nebula is very similar in the UKIRT and Subaru datasets.

If we adopt P.A.=35° as the orientation of the disc axis (this being the orientation of the minor axis of the millimetre disc observed by Mundy et al.(1996); Wilner et al.(1996)) then the data in Table 1 indicate that the polarisation vectors associated with the point source are inclined by between 32° and 43° to the disc axis. The polarised flux maps suggest P.A.=46° ± 8° for the disk axis (see above) and the orientation of the optical jet (Mundt et al. 1990) suggests P.A.≈ 50°. These values (and casual inspection of Figure 5(a-c)) would suggest a slightly smaller inclination to the disc axis. However they are derived from or influenced by the distribution of matter in the outflow cavities, which may not be ejected along the disc axis.

Table 1 - Polarisation of the central point source

Data	P.A.	Polarisation
UKIRT K band	79.7°	3.3% ± 0.3%
UKIRT H band	77.4°	3.7% ± 0.3%
Subaru K band	68.5°	6.8% ± 1.7%

Note: polarisation is measured in a 0.4 arcsec diameter aperture centred on the point source.

The polarisation of the point source is interpreted as the result of dichroic extinction of light from the protostar by aligned non-spherical grains. This interpretation is supported by the observation of a distortion of the centrosymmetric pattern between at distances from 0.5 and to 1.5 arcsec from the point source which is consistent with a dichroic extinction pattern that is superimposed upon the centrosymmetric pattern produced by scattering. The apparent dichroic extinction seen at H and K produces polarisation at P.A.$\approx 79°$ (see Table 1), which would be expected to add to the scattering-induced polarisation at locations north of the protostar, but subtract from the scattering-induced polarisation to the east of the protostar. Cuts across the disc axis in the approaching lobe are shown in Figure 6, illustrating that there is a polarisation gradient across the axis at J band.

This behaviour is observed at J band on scales up to 1.5 arcsec (~ 200 AU) from the flux peak (which is offset slightly from the protostar, see section 5), and is attributed to dichroic extinction of scattered light passing through the dense inner parts of the envelope. It is possible that the polarisation gradient across the disc axis relates at least in part to structural asymmetries of the nebula however. The same distortion is apparently observed at H and K band in the data from both telescopes but that might be simply due to contamination by direct flux from the bright nearby protostar (the central point source) in the wings of the image profile. Light which is scattered within ~ 100 AU of the protostar will experience a dichroic extinction similar to that of direct flux from the photosphere or hot accretion disc. This interpretation and the information derived about the magnetic field by Monte Carlo modelling are discussed further in Section 5.

The observed polarisation structure is unusual, though only a few YSO have been subject to polarisation measurements at this high spatial resolution. Class I YSOs commonly exhibit a region of aligned vectors near the projected location of the protostar. These are usually aligned with the disc plane, and are often interpeted in terms of polarisation dominated by double scattering, due to high optical depth on the line of sight to the central source (Whitney & Hartmann 1993; Bastien & Menard 1988). Aligned vectors have occasionally been observed in less embedded Class I sources similar to HL Tau, where the protostar is seen directly through a lower optical depth ($\tau < 6$). For example, LR98 observed a 'polarisation disc' aligned parallel to the disc plane of TMR-1, which has a bright central flux peak.

On larger scales the polarisation pattern of HL Tau is approximately centrosymmetric, though the centrosymmetry is imperfect in places due to the effects of both double scattering and the finite width of the image profile: polarisation measured in areas of faint nebulosity is contaminated by the polarisation signal from adjacent areas of brighter nebulosity. The maximum polarisation measured in the outer nebulosity in a 0.24 arcsec aperture is 80% in the K and H bands in the UKIRT data, and 75% in the Subaru K band data. The maximum polarisation measured in the UKIRT J band data is 75%.

4 MONTE CARLO LIGHT SCATTERING CODES

Three Monte Carlo codes were used to investigate the 3-D structure of the envelope around HL Tau and the structure of the magnetic field, which is inferred from the direction of grain alignment. The first code, 'range_asph.f' is a 2-D code used to model YSOs which are symmetric about the axis of the accretion disc and the envelope (axisymmetric). The code is described in Lucas (2003). It incorporates scattering by oblate spheroids which are perfectly aligned with an arbitrary magnetic field structure. This is an extension of the code used by LR98 ('range.f') to model scattering by spheres, with the non-spherical particles allowing us to include the effects of dichroic scattering and dichroic extinction on model images and model polarisation maps. This code has been qualitatively bench tested against that of Whitney & Wolff (2002). The T-matrix code ampld.f of Mishchenko, Hovenier & Travis (2000) is used to generate the large look up tables required to calculate both the polarisation after each scattering of a photon and the phase function from which the scattering direction is sampled by rejection sampling. The range_asph.f code was used with a uniform axial magnetic field to constrain the basic parameters of HL Tau, such as system inclination, optical depth and the approximate axis ratio of the oblate grains, before moving to a 3-D analysis.

The second code, 'whale.f', is a very simple extension of range_asph.f to 3-D, which was used to model the non-axisymmetric matter in the cavity of HL Tau. The great drawback of such a 3-D code in which the photons are randomly scattered is that only a small fraction of the photons used by the code are output into the direction of observation. In 2-D axisymmetric codes all photons can be assumed to exit at the correct azimuthal angle for observation, and output photons are binned only by polar angle (corresponding to different system inclinations). Run times of 7 hours were required with 8 CPUs on a fairly fast parallel SGI Origin 2000 computer to produce rather poor quality model images from an initial 20 million photons originating at the photosphere. Despite this drawback whale.f is useful to explore the range of possible orientations of the system, since the output can be used to make images for any direction of observation. In range_asph.f and whale.f the photons at first have no chance for absorption during a scattering event. Instead the more efficient process of multiplying the Stokes vector of each photon by a weighting factor is used. The weight is given by:

(1) $\text{W} = \omega^N$

where ω is the albedo and N is the number of times the photon has been scattered. Absorption of photons is not permitted until W$< 10^{-3}$, whereupon the weight is held

constant and absorption or scattering occurs in the natural random manner.

Following discussions with K. Wood (private comm.) a third code was written, 'shadow.f', which uses the technique of forced scattering to permit much faster 3-D modelling. The forced scattering technique is described by Cashwell & Everett (1959); Yusef-Zadeh, Morris & White (1984) and Wood & Reynolds (1999), for application to scattering by spheres. Photons propogate along random multiple scattering paths until they exit the system, as in whale.f. However, every time a photon scatters, a 'shadow photon' is generated at the scattering location and propogates into the user specified observation direction. The shadow photons penetrate any optical depth and never scatter, so they are weighted according to the probability of such an event. Each shadow photon therefore has a weight:

(2) $W = \omega^N \, P(D,\gamma) \, e^{-\tau}$

where N is the number of times the parent photon has been scattered; $e^{-\tau}$ is the probability of a photon travelling the corresponding optical depth τ to the edge of the system without scattering or absorption; and $P(D,\gamma)$ is the probability of scattering through the corresponding deflection angle D and azimuthal angle γ. The azimuthal deflection angle γ is defined as a left handed rotation about the Poynting vector of the parent photon, with zero at the incident polarisation position angle. $P(D,\gamma)$ is a function of the grain mixture (size distribution and shape), grain orientation and the (IQUV) polarisation state of the incident photon. Shadow.f is far more efficient than whale.f, with speed closer to a 1-D code than a 3-D code. Calculation times of only 6 minutes with 8 CPUs were required to generate high quality models, using only 10^5 photons (with one caveat, see below). Forced scattering codes such as this have different statistical properties than fully stochastic codes. They provide a more 'democratic' spread of model image quality due to the penetration of high optical depth by shadow photons. The signal to noise in the obscured receding lobe of a bipolar nebula is similar to that of the bright approaching lobe. This code was used to refine models of the following: (i) the magnetic field structure in the envelope; (ii) the matter distribution in the envelope and the bipolar cavity; and (iii) the near infrared extinction law and the grain axis ratio.

Shadow.f was coded by adding a single subroutine to whale.f to handle the shadow photons. Two complications are worthy of mention. The first is that the output flux of shadow photons is not normalised relative to the direct (unscattered) flux from the protostar. This is significant in cases like HL Tau where the protostar is directly observed through a modest optical depth. The normalisation was handled by causing shadow.f to produce the traditional stochastic output of whale.f as well as the forced output. The ratio of direct flux to total scattered flux in the stochastic output was then used to determine the appropriate direct flux in the shadow photon images. A reasonably precise normalisation (better than 10% precision) required longer runs with 10^6 photons.

The second complication of shadow.f is a difference between the phase function for forced scattering and that for stochastic scattering. The phase function for forced scattering is the probability $P(D,\gamma)$ per unit solid angle, whereas the phase function for stochastic scattering is $P(D,\gamma)sin(D)dDd\gamma$, incorporating the amount of solid angle in a bin of width $dDd\gamma$ at deflection angle D. The need to remove the $sin(D)$ term was discovered during exhaustive bench testing to provide precise quantitative agreement between outputs from shadow.f and whale.f. The testing used a homogeneous sphere with a uniform magnetic field, a homogeneous sphere with a pinched and twisted field, and a model of HL Tau.

The phase function used in shadow.f is:

$$(3) \, P(D,\gamma) = \{0.5(1-LP)(|S_{11}|^2 + |S_{12}|^2 + |S_{21}|^2 + |S_{22}|^2)$$

$$+LP[(|S_{22}|^2 + |S_{12}|^2)sin^2(\gamma) + (|S_{11}|^2 + |S_{21}|^2)cos^2(\gamma)$$

$$+sin(2\gamma)Re(S_{11}S_{12}^* + S_{22}S_{21}^*)]$$

$$-CP(Im(S_{11}S_{12}^* - S_{22}S_{21}^*))\}/T(\alpha_0,\beta,LP,CP)$$

where the S_{ij} terms are $S_{ij}(\alpha,\beta,D,\gamma)$, the (complex) elements of the 2×2 amplitude matrix used to calculate the scattered components of the electric field parallel and perpendicular to the scattering plane (eg. Mishchenko et al.2000). As described in Lucas (2003), α and β are the azimuthal and polar grain orientation angles in the frame of the incident photon. LP and CP are the fractional linear polarisation and circular polarisation of the incident (parent) photon. To reduce the size of the look up tables for the S_{ij} arrays, the photon azimuthal deflection angle γ is set to zero in the S_{ij} elements and α (the grain azimuthal orientation angle) is calculated relative to the azimuthal deflection. The numerator in Eq.(3) is the scattered flux per unit solid angle. The denominator $T(\alpha_0,\beta,LP,CP)$ is used to normalise the scattered light intensity as a probability function. $T(\alpha_0,\beta,LP,CP)$ is the sum of the numerator in Eq.(3) evaluated over all possible scattering angles (D,γ), for the combination of (α_0,β,LP,CP) appropriate to the parent photon. The term $\alpha_0 = \alpha - \gamma$. It represents the azimuthal orientation of the grain perceived by the incident photon, relative to the polarisation plane, correcting for the fact that α is defined relative to γ. (Note that α rather than α_0 was erroneously used in Lucas (2003) in the normalisation term '$IMAX(\alpha_0,\beta,LP,CP)$' for the phase function in the stochastic code range_asph.f. However testing indicates the error was too subtle to have any measurable effect on model results).

Image Convolution

The (IQUV) maps produced by the above codes have to be convolved with a point spread function (PSF) which is the best available match to the image profile yielded by the telescope. The PSF for Subaru/CIAO was determined by fitting a field star observed shortly after HL Tau with a moffat profile in the IRAF software package. No suitable reference data was obtained during the UKIRT Service observations of HL Tau on the same night, so the rebinned image profile based on similarly out of focus data from the previous night (see right panel of Figure 1) was used as the basis for the convolution kernel. The effective spatial resolution on that night was approximately 0.65 arcsec. However, after convolving with the J, H and K band models this resolution was slightly too poor to reproduce much of the fine structure seen in the data, such as the double peaked profile of the J band polarised flux data in Figure 4(b). The convolution

kernel was demagnified by varying amounts to give effective resolutions ranging from 0.4 to 0.65 arcsec to assess the true resolution. Models with resolutions ranging from 0.4 to 0.6 arcsec were found to fit the data, although 0.5 to 0.6 arcsec resolution is most likely due to the defocussing. A kernel with a resolution of 0.55 arcsec was therefore adopted and used in the models of the UKIRT data. The uncertainty in the true spatial resolution of the UKIRT J band data increases the uncertainty in the fitted J band optical depth and the derived extinction law in section 5.

5 MODELLING HL TAU

5.1 Initial assumptions and prior data

The protostar is assumed to be surrounded by a physically thin but flared accretion disc in hydrostatic equilibrium (Shakura & Sunyaev 1973), described by:

$$\rho_{disc} = \rho_0(r/R_*)^{-15/8} exp[-0.5(z/h)^2]; \quad R_D > r > R_{min}$$
$$(4) \qquad = 0; \; r < R_{min}$$
$$\qquad = 0; \; r > R_D$$

where r and z are cylindrical coordinates defined by the disc plane and h is the disc scale height, given by:

$$(5) \quad h = h_0(r/R_*)^{9/8}; \quad h_0 = R_*/75$$

where R_* is the stellar radius, set at 2 $R_\odot$ (or $\sim$ 0.01 AU). The small dust grains observed in the near infrared are assumed to be well mixed with the gas. The accretion disc may contribute to the K band emission, providing a different angular distribution of photons than the spherical protostar. The dust disc is assumed to have an inner hole within radius R_{min} due to disc disruption or dust sublimation. Default parameters of $R_{min} = 2R_*$, $R_D = 150 \, AU$ and zero thermal contribution from the disc were adopted. In practice the structure of the accretion disc and any thermal flux have very little effect on the model output, which is dominated by the larger scale envelope and the bipolar cavity.

For the larger scale envelope two density structures were investigated, described by Eqs.(6) and (7):

$$\rho_{env} = C/R^{1.5}[1/(((|z|/R)^v +0.05)]; \quad R_{cav} < r < 1300 \, AU$$
$$(6) \qquad = 0; \; r < R_{cav}$$

where $R = \sqrt{r^2 + z^2}$, C is a free parameter governing the optical depth and the power law index v is a parameter describing the vertical gradient of the envelope. $v = 0$ correesponds to spherical symmetry, while increasing to positive values causes progressively more flattening of the envelope. R_{cav} is the radius of the evacuated conical cavity in the disc plane, for which an opening angle $\theta_c = 45°$ to the disc axis was adopted in the initial model. Eq.(6) is a simple, empirically derived formalism, adopted following the discovery that the $R^{-1.5}$ power law seems to extend throughout the envelope in at least some YSOs (LR98).

$$\rho_{env} = \frac{\dot{M}}{4\pi} \frac{1}{(GM)^{1/2}} \frac{1}{R^{3/2}} \frac{1}{(1+\mu/\mu_0)^{1/2}} \frac{1}{(\mu/\mu_0+2\mu_0^2 c_r/R)};$$
$$R_{cav} < r < 1300 \, AU$$

$$(7) \quad = 0; \; r < R_{cav}$$

where M is the mass of the protostar, $\dot{M}$ is the accretion rate, $\mu = |z|/R$ and $\mu_0 = $ f(r/c$_r$, μ) (see Whitney & Hartmann 1993). Eq.(7) is the inner solution of Terebey, Shu & Cassen (1984) for the inside out collpase of a rotating singular isothermal sphere, also derived by Ulrich (1976). Eq.(7) differs from Eq.(6) primarily in the radial density profile: at radii much greater than the 'centrifugal radius' c$_r$, the density profile varies as R$^{-3/2}$, but at smaller radii the density varies more slowly, as R$^{-1/2}$ for R $<<$ c$_r$. The density distribution is nearly spherical at R $>>$ c$_r$ but becomes flattened at smaller radii. The outer limit to the system is set at 1300 AU in both formalisms, since this is the approximate extent of the observed millimetre and infrared structures (eg. Hayashi et al.1993).

In the initial model the cavity structure was assumed to be conical and perfectly evacuated, with a radius of 25 AU in the disc plane, with an opening angle of 90°.

Two important parameters in the model fit are the system inclination and the optical depth to the central star. The most direct mean of determining the inclination is from the elongation of the disc seen in the millimetre continuum. Those observations which have clearly resolved the disc with a P.A. near 125° imply inclinations $i = 60^{\circ +14}_{-16}$ (Mundy et al.1996 at 2.7 mm), $i = 62^{\circ +9}_{-10}$ (Wilner et al. 1996 at 7 mm). High resolution ^{13}CO maps by Hayashi et al.(1993) imply $i \approx 67°$, though the inference from CO data is less direct. Close et al.(1997) adopted $i = 67°$ in their Monte Carlo model. By contrast, Menshchikov et al.(1999, hereafter MHF99) prefer a much lower value ($i = 43°$), which follows from their adoption of a model with a physically thick inner torus on a 100 AU scale, as opposed to our more conventional physically thin inner accretion disc on a similar scale. The thick torus model put forward by MHF99 for Class I YSOs is thought provoking, even though simplified by its essentially 1-D nature (see Menshchikov & Henning 1997 for the computational details). MHF99 modelled the entire optical to centimetre waveband SED of the system with a 4-component, spatially segregated dust model. They also modelled low resolution imaging polarimetry with the Monte Carlo method, though with limited quantitative success. This model of a thick inner disc which is not yet in hydrostatic equilibrium cannot be entirely ruled out but we consider such a thick torus (with the surface rising linearly at 45° from the disc plane) to be unlikely for the following reasons: (i) the high elongation of the disc observed in the millimetre waveband on several occasions argues strongly for a large inclination of the system, almost certainly with $i > 45°$; (ii) their fit requires that the line of sight passes very close to the cavity wall as viewed in the near IR, which is something of a coincidence; (iii) the observation of an unresolved central source at 2 μm here and in Close et al.(1997) suggests that the protostar is observed directly, contrary to their model; and (iv) millimetre wave mapping and Monte Carlo modelling of IRAS 04302+2247, another Class I YSO in Taurus believed to be at a similar evolutionary stage, observed at i=90° (eg. Wolf et al. 2003; LR97) has preferred flatter disc models. LR97 discounted thick discs on a 100 AU scale because these were detectable and very prominent in high resolution Monte Carlo maps but not seen in the data.

The optical depth to the central source is not known a

priori. Close et al.(1997) provide point source fluxes at J, H and K, though with significant uncertainty at J band due to the difficulty of precisely subtracting the scattered light contribution. If the extinction law is known the K band optical depth τ_K can be derived from the (J-H) colour excess, assuming this is almost entirely caused by extinction. We take the (J-H) colour of the photosphere to be 0.58, using the derived temperature T_{eff} = 4600 K of Close et al. and the colours of Tokunaga (2000). (The colours are the same for Class III and Class V stars, and are only a weak function of T_{eff}). Hence E(J-H)=2.59. Adopting the $\lambda^{-1.61}$ near infrared extinction law of Cardelli, Clayton & Mathis (1989) leads to A_K = 2.89 mag or τ_K = 2.66. Adopting the shallow extinction law suggested by LR98 for Class I YSO envelopes in Taurus leads to A_K = 5.63 mag or τ_K = 5.18. Values between these two extremes were explored in the simulations.

The magnetic field was initially assumed to be uniform and parallel to the disc axis. The more complicated structures required to fit the polarisation maps in the vicinity of the protostar are described in section 5.2.2.

5.2   The successful model

The parameters of the successful model are summarised in Table 2 and it is illustrated in Figure 7 with the disc axis oriented vertically. The features which the model fits are:

(1) Quantitatively, the ratio of polarised flux in the brightest part of the receding lobe to that at the central polarised flux peak, evaluated in the J, H and K bands. A 0.4 arcsec aperture was used for the measurements. The measured ratios in the UKIRT data are 0.065 at K band, 0.11 at H band, and $\sim$ 0.05 at J band. The ratios in the Subaru H and H band data are the same after accounting for the higher polarisation of central flux peak in the Subaru data. The prominence, location and well defined boundaries of the receding lobe in polarised flux could only be fitted with a component of dust in the receding lobe of the outflow cavity.

(2) Quantitatively, the offset along the disk axis of the J band peak in total flux from the centre of the polarisation pattern, as defined by the polarisation nulls southwest of the flux peak. The nulls are used since there is no clear 'polarisation disc' and no unique focus for the centrosymmetric vectors in the outer nebulosity.

(3) Quantitatively, the radial profile of the K band flux image, along a cut extending along the disc axis from the protostar to the edge of the approaching lobe. This feature is fitted using the Subaru data, for which the image profile was well defined by observation of a stellar standard (see Section 4).

(4) Quantitatively, the maximum degree of polarisation in the HL Tau nebula at J, H and K, evaluated in a 0.24 arcsec aperture.

(5) Quantitatively, the position angle and percentage of the K band polarisation of the central point source. The magnitude and structure of the polarisation vectors around the protostar are also reproduced well in the H and J bands.

(6) Qualitatively, the distortion of the centrosymmetric pattern within 100 AU (0.7 arcsec) of the protostar by dichroic extinction of scattered light, observed at J, H and K (see Figure 6). A quantitative fit was not attempted owing

to the uncertainties caused by sensitivity to the convolution function used to smooth the models.

(7) Qualitatively, the presence of the broad scattering peak called Source B, seen in polarised flux at J, H and K and modelled with dust in the approaching lobe of the bipolar cavity. Source B is most clearly seen in the J band model.

(8) Qualitatively, the presence of the filament of nebulosity extending north of HL Tau in Figure 3(c), interpreted as a limb brightened cavity wall of the approaching lobe.

(9) Qualitatively, the shape of the bipolar nebula in the polarised flux images. This is reproduced better by curved cavity walls (in the parabolic sense) than by a conical cavity profile. In addition the modest indentation of the contours in the dark lane southwest of the protostar is better fitted by dust grains with a fairly high albedo ($\gtrsim$ 0.3 at H and K), since significant multiple scattering permits stronger illumination of the equatorial plane of the envelope, which is optically thick at low latitudes (see Figure 14 of LR98).

Table 2 - Parameters of the Successful Model

Parameter	Value
System Radius	1300 AU
Optical Depth to the protostar at J, τ_J	$7.10^{+1.31}_{-0.45}$
Optical Depth to the protostar at H, τ_H	5.25 ± 0.35
Optical Depth to the protostar at K, τ_K	3.75 ± 0.50
envelope vertical density gradient, v	0.65 ± 0.15
grain axis ratio, gr	$1.015^{+0.015}_{-0.005}$
system inclination, i,	$66° < i < 71°$
cavity radius in disc plane, R_{cav}	25 AU
*cavity opening angle, θ_c	$45°$
*cavity curvature parameter, cc	$0.1^{+0.2}_{-0.1}$

* The cavity profile is described in Eq.(8). The opening angle is defined relative to the disc axis.

5.2.1   Structure of the circumstellar matter

Two modifications to the initial structural assumptions of Section 5.1 were required to produce this fit. First, dust in both lobes of the cavity (not merely within the cavity walls) was required to fit the prominent and well defined receding lobe seen in polarised flux (Figure 2(b,d); Figure 3(b,c)), and the diffuse Source B in the approaching lobe. For simplicity this dust is assumed to have the same properites as the dust in the envelope and the disc (see section 5.2.3). The dust distribution used in the receding lobe is axisymmetric and located at $200 < R < 400$ AU. The optical depth along the disc axis in the receding lobe is $\tau \sim 2$ at K band, which maximises the lobe brightness. An R^{-2}, approximately 'constant flow' density distribution provides the best qualitative match to the data. The dust in the approaching lobe has to be non-axisymmetric to reproduce Source B and explain why only one limb of the cavity wall is observed. This dust component was simplistically modelled using a uniform density distribution of dust filling one half of the cavity between 160 and 360 AU from the protostar. In the model coordinate system this dust location within the cav-
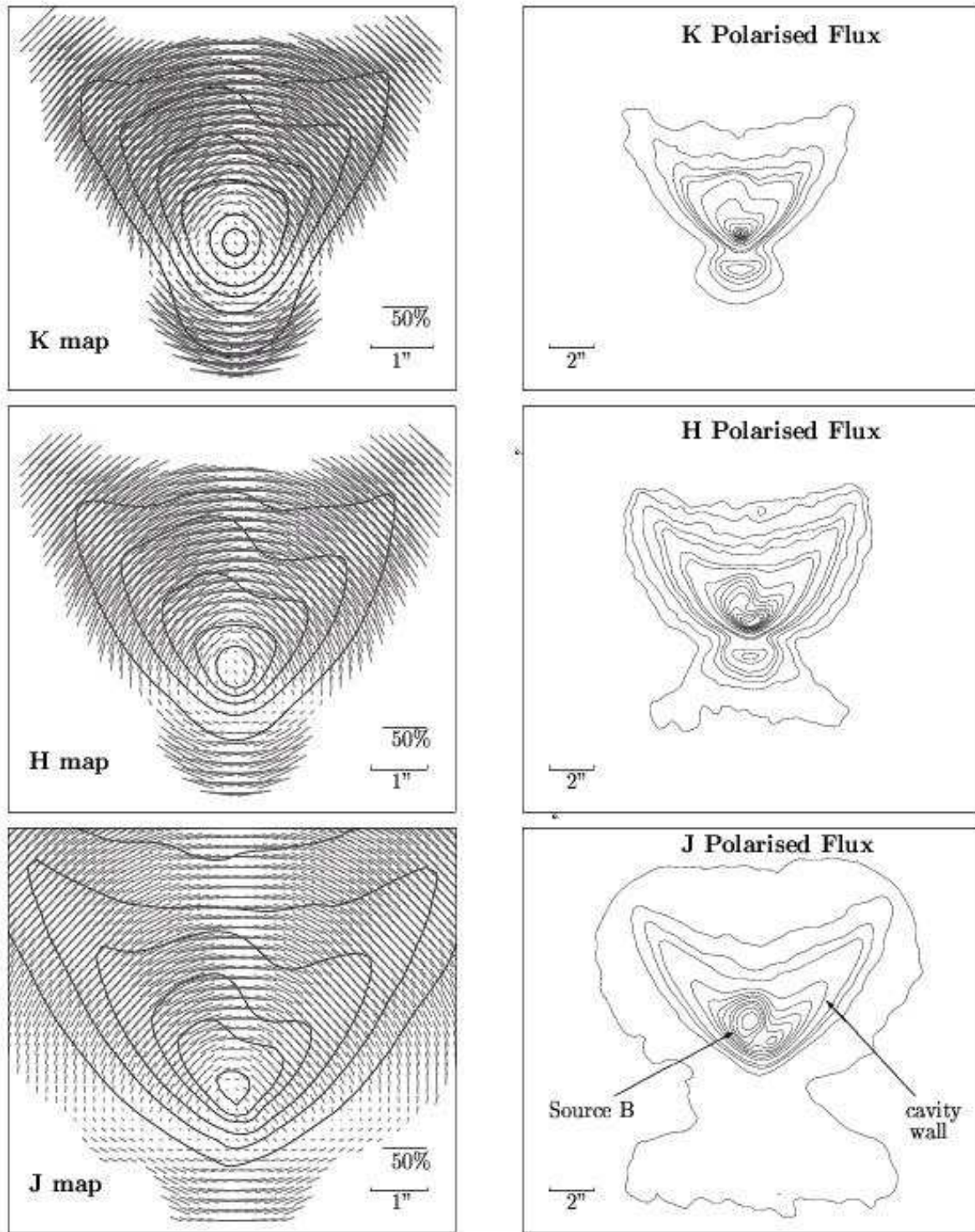
Figure 7. Successful model. (top) K band; (middle) H band; (bottom) J band. Left panels show the model images and polarisation maps, including only the central regions for clarity. The pixel scale is 0.15 arcsec, corresponding to 21 AU in the system. Right panels show polarised flux images of the whole system with similar dynamic range to the data. The K and H band models are smoothed to the 0.4 arcsec resolution of the Subaru data, while the J band model is smoothed to the 0.55 arcsec resolution of the UKIRT data (see section 4). All contours are normalised to unity at the peak. Contour levels in the polarisation maps areas follows. K band: 0.5, 0.16, 0.03, 0.015, 0.0075, 0.0038. H band: 0.5, 0.25, 0.125, 0.0625, 0.031. J band: 0.9, 0.85, 0.43, 0.21, 0.11, 0.053. The polarised flux images have the following contour levels. K band: 0.01, 0.02, 0.03, 0.04, 0.05, 0.1, 0.2, 0.3, 0.4, 0.5, 0.6, 0.7, 0.8, 0.9. H band: 0.015(2), 0.02, 0.03, 0.04, 0.05, 0.08, 0.1, 0.2, 0.3, 0.4, 0.5, 0.7, 0.8, 0.9. J band: 0.01(2), 0.04, 0.07, 0.1, 0.2, 0.3, 0.4, 0.5, 0.62, 0.7, 0.8, 0.9. The '(2)' indicates contouring of 2×2 binned pixels.

ity is $160 < R < 360$ AU, $-150° < \Lambda < -45°$, where Λ is the azimuthal coordinate, defined as a right handed rotation about the disc axis with an arbitrary zero point. An azimuthal viewing angle of $\Lambda = 45°$ then qualitatively reproduces Source B so this is the adopted viewing angle for the successful model. The optical depth close to the disc axis in the approaching lobe is $\tau \sim 0.36$ at K band, the dust density being somewhat lower than in the receding lobe. Note that a precise 3-D fit to the distribution of cavity dust is not possible with 2-D data, so this aspect of the model is only approximate.

Second, the conical profile of the cavity walls produce a slightly smaller offset of the flux peak at J band than was observed and the overall shape of the nebula lacks the curvature seen in the data at J, H and K. As noted in section 3, the protostar is slightly offset from the centre of the polarisation pattern (as defined by the nulls) due to the inclination of the system (see LR98). The data show an offset along the disc axis of 0.40 ± 0.11 arcsec from the nulls to the flux peak. The shift in the models is somewhat dependent on the spatial resolution of the convolution kernel so a conical profile could not be ruled out. However the conical profile successfully fits the J band data only for a very small region of the parameter space in optical depth and vertical density gradient. Hence, a curvature parameter, cc, was introduced to create an approximately parabolic cavity profile, as described by Eq.(8). A parabola-like profile causes the inner parts of the cavity to subtend a larger solid angle to radiation from the protostar than a conical profile; the inner part of the cavity then becomes brighter, causing a greater shift of the flux peak at J band. The total offset in the successful model is therefore composed of 0.15 arcsec from the nulls to the protostar and a further 0.25 arcsec from the protostar to the flux peak. Note that it was also possible to reproduce the J band offset by introducing a knot of dust in the cavity at the observed location of the flux peak, but this did not reproduce the distortion of the J band polarisation pattern which we attribute to dichroic extinction.

(8) $((r - R_{cav})/|z|)(R/R_{cav})^{cc} = tan(\theta_c)$

Effects of model parameters

As noted in Section 4, the strong wavelength dependence of the receding lobe in polarised flux and the offset of the J band flux peak from the centre of the polarisation pattern are powerful constraints upon the model. The 'rotating singular isothermal sphere' density distribution in Eq.(7) failed to simultaneously reproduce the observed flux and polarised flux ratios of (i) central peak:receding lobe and (ii) central peak:Source B, for any centrifugal radius in the range $0 < c_r \leq 1000$ AU. The failure was worst at J band, where the observed structure could not be even qualitatively reproduced. The principal difference between the two density distributions of Eq.(6) and Eq.(7) is in the vertical density gradient. Eq.(6) has a radius-independent vertical density gradient which appears to fit the data better. This radius-independent flattening might be consistent with influence of the magnetic field, causing collapse of the envelope along field lines to produce a large disc-like structure.

In summary the effects of the more important parameters are:

(1) v (the power law index controlling the vertical density gradient of the envelope (flattening)). Increasing v causes the receding lobe to become fainter at all wavelengths.

(2) gr (grain axis ratio). Increasing the grain axis ratio to make progressively more oblate spheroids increases the polarisation of the protostar by increasing the amount of dichroic extinction. $gr = 1.015$ fits the ~ 3 to 4% polarisation observed with UKIRT at H and K (see Table 1) when combined with the adopted magnetic field structure (see below). $gr = 1.03$ is required to fit the larger polarisation (6.8%) of the protostar measured by Subaru at K band but it should be noted that the 2 telescopes agree within the measurement errors (see Section 3). gr would be slightly smaller in the case of a uniform field but could be much larger if the grains are not perfectly aligned.

(3) τ_K (envelope optical depth at K band). Values of this parameter in the range $2.66 < \tau_K < 5.18$ were explored (see section 5.1). The nebulosity in the Subaru data appears to have a shallower radial profile than the model: optical depths in the range 3.25 to 4.25 reproduce the flux at radii which increase with decrasing optical depth. This suggests that either the radial density gradient of the envelope is less steep than $\rho \propto R^{-1.5}$ or there is additional diffuse dust in the cavity, not included in the model, which increases the flux at larger radii. Given the apparent asymmetry of the nebulosity the K band optical depth cannot be more tightly constrained via the radial profile.

(4) τ_H (envelope optical depth at H band). The very prominent receding lobe seen in H band polarised flux tightly constrains the H band optical depth to $\tau_H = 5.25 \pm 0.35$, provided that system inclinations i consistent with the millimetre observations are employed (see below). At larger values of τ_H the receding lobe becomes fainter as the dense disc plane obscures it. At smaller values the central peak of the nebula is unresolved in polarised flux, indicating that it is dominated by direct flux from the protostar. This contrasts with the data from both telesceopes in which the central peak is diffuse in polarised flux. At still smaller values, $\tau_H < 4.5$, the receding lobe again becomes relatively fainter as the protostar becomes more and more prominent.

(5) τ_J (envelope optical depth at J band). This parameter is constrained by the prominence and spatial offset of the principal scattering peak observed in total flux, by the faintness of the receding lobe, and by the diffuse double peaked structure seen in polarised flux (Figure 4(b)). Raising the optical depth above the preferred range reduces the prominence of the 'principal' scattering peak relative to the more diffuse polarised flux peak, Source B. High optical depth also makes the receding lobe fainter and can increase the spatial offset. At $\tau_J > 8.4$ Source B becomes much brighter than the 'principal' peak. At low optical depth, $\tau_J < 6.65$, the receding lobe becomes too bright in diffuse flux and the knot seen at H and K becomes visible at J band, in contrast to the data.

(6) cc (cavity curvature). The best fit value is 0.1. Increasing cc increases the spatial offset of the J band flux peak when the empirical envelope density function is used. A positive value of cc (i.e. a more parabolic cavity) also

qualitatively fits the curved morphology of the polarised flux images better than a conical cavity.

(7) θ_c (cavity opening angle). This parameter is not tightly constrained since the values in the range $\theta_c = 45° \pm 10°$ produce acceptable results, and there is some degeneracy between θ_c and the curvature parameter, cc.

(8) albedo, ω. The albedo of the dust grains was treated as a free parameter (see 5.2.3). Increasing the albedo increases the prominence of the receding lobe observed in polarised flux, relative to the central peak in polarised flux. The ratio of polarised fluxes does not rise linearly with albedo however; instead a weaker, approximately square root dependence is seen in the models. This behaviour is seen in simulations at all 3 wavelengths, even though the central peak in polarised flux is slightly offset from the location of the protostar seen in total flux (the central point source). For models with inclination $i = 66°$, an albedo of ≈ 0.6 is preferred to precisely match the prominent receding lobe at H band. However after allowing for the possibility of a slightly larger system inclination and the fairly weak albedo dependence of the solution, the data are consistent with $\omega \gtrsim 0.4$ at H and $\omega \gtrsim 0.2$ at K. The high albedo also helps reproduce the morphology of the nebula in polarised flux (see model feature 9 above.)

(9) system inclination, i. The inclination derived from the elongation of the inner accretion disc seen in the millimetre continuum is $62°^{+9}_{-10}$, adopting the most precise available determination by Wilner et al.(1997) (see section 5.1). However simulations with $i \approx 62°$ fail to reproduce the positional shift of the J band flux peak and make the receding lobe much too faint in all 3 wavelengths. The minimum inclination which produces a successful Monte Carlo fit is $i \approx 66°$. Inclinations of $70°$ or more can also produce successful fits to most of the near infrared data but become less consistent with the millimetre data quoted above. The receding lobe also becomes too bright at J band for inclinations much in excess of $70°$. The preferred inclination is therefore $66° < i < 71°$. Close et al.(1997) preferred the similar value of $67°$ in their Monte Carlo simulation, in agreement with the value derived from [13]CO mapping by Hayashi et al.(1993).

5.2.2 Structure of the magnetic field

Polarisation vectors inclined by between $32°$ and $43°$ to the disc axis are observed at the location of the protostar in the H and K bands. This can be simply reproduced by dichroic extinction by grains aligned with a magnetic field which is globally misaligned with the disc axis. This would imply a field orientation of $122°$ to $133°$. A globally misaligned field cannot be ruled out without spatially resolved circular polarimetry but an explanation more consistent with star formation theory is that the field is pinched and twisted by the collapse of the rotating molecular cloud core from which the presently observed envelope descended. Such a twisted magnetic field in the circumstellar structure near the central star is consistent with that predicted from the millimeter polarization data (Tamura, Hough & Hayashi 1995) although their detection is marginal.

We have constructed an empirical formalism for a pinched and twisted field similar to the 'split monopole' configuration described in recent MHD simulations by Allen, Li & Shu (2003). A detailed fit to the MHD simulations will not be attempted until better quality circular polarisation data is obtained. The split monopole indicates the discontinuity in the direction of the field lines in the disc plane, which implies the presence of a current sheet. Field lines are assumed to be dragged away from an initially axial direction by the rotation of the disc and envelope.

The adopted formalism is:

(9) $B_r = b_1 z/|z| r^m exp(-(r^n + a|z|))$

(10) $B_z = b_0 + b_1/ar^{m-1} exp(-(r^n + a|z|))(m + 1 - nr^n)$

(11) $B_\phi = b_2 z/|z|(1/(r^q + az^q + c))$

where b_0, b_1, b_2, a, c, n, m and q are positive constants which parameterise the field structure. One additional parameter is the unit of length L_B by which the cylindrical polar coordinates r and z are normalised. B_ϕ is the field strength in the azimuthal direction perpendicular to the **r** and **z** vectors. This formalism was also used in Lucas et al.(2003).

At large radii ($R \gg L_B$) the field becomes axial ($B_z \rightarrow b_0$, $B_r \rightarrow 0$, $B_\phi \rightarrow 0$). The signs of B_r and B_ϕ reverse in the plane of the accretion disc (z=0) where the pinch and twist is strongest. The form of B_z relates to B_r in a manner constrained by the divergence equation. By contrast B_ϕ, the twist component, is independent of the other components since the twist is axisymmetric and therefore does not contribute to the divergence equation.

Figure 8 depicts an example of a field structure which successfully reproduces both the $43°$ inclination of the polarisation of the protostar seen in the UKIRT data and the observed distortion of the centrosymmetric pattern, with the spatial scale in units of L_B.

The most important parameters in successful field solutions are the coefficients $b0$, $b1$ and $b2$. and the scale length L_B. The successful model fit in Figure 7 has a cavity radius, $R_{cav} = 25$ AU in the disc plane, though this parameter is not tightly constrained. Exploration of the magnetic field parameter space for this adopted cavity size indicates that for parameters ($b0, b1, b2 = 0.5, 1.5, 2.0$, a scale length
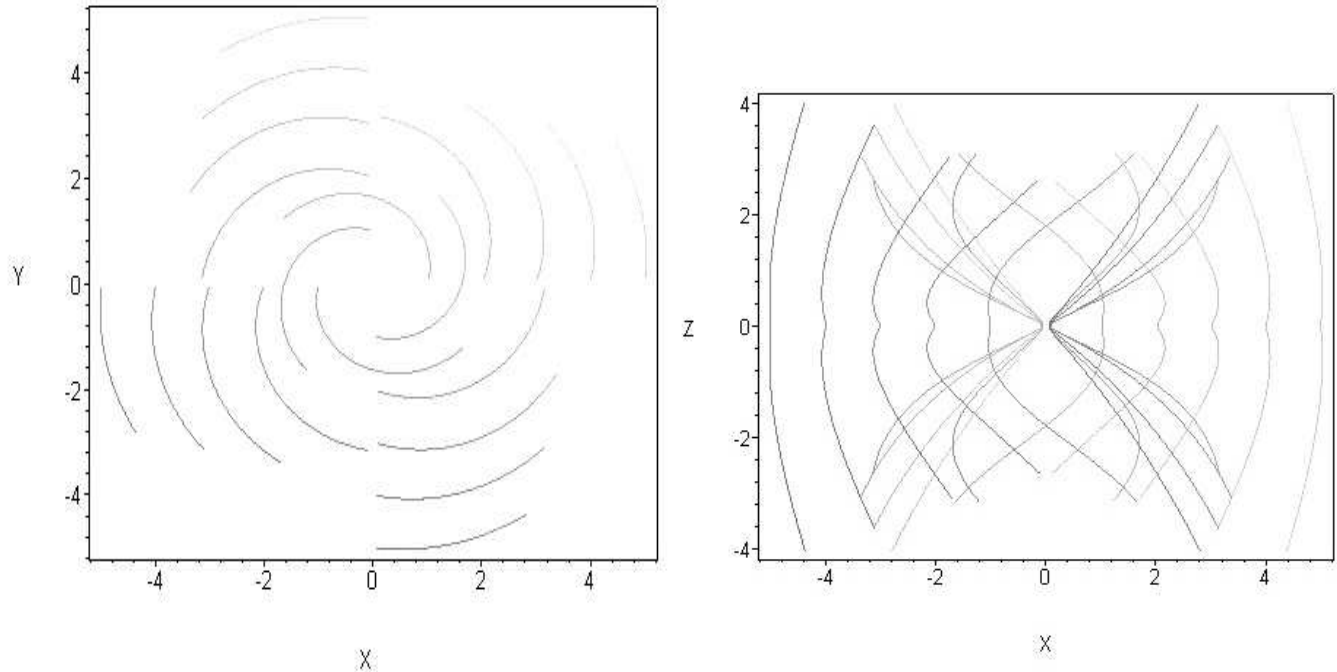
Figure 8. Field structure for parameters $(n = 1, m = 1, q = 1, a = 0.4, b0 = 0.5, b1 = 1.5, b2 = 2.0, c = 0.1)$, see Eqs.(9-11). The field lines are highly twisted and also somewhat pinched. (left) view of the field lines looking down on the disc plane. (right) view from the disc plane, showing the pinch more clearly.

$L_B \gtrsim 15$ AU is required to reproduce the $32°$ to $43°$ inclination of the polarisation of the protostar, this being only weakly dependent on the power law indices n and m. This suggests that while the twist of the field must obviously extend into the dense inner part of the circumstellar envelope if it is to have a large effect on the dichroic extinction, it need not fill most of the volume of the 1300 AU structure. The polarisation gradient across the sytem axis observed at J band (see Figure 6) extends to distances of more than 100 AU from the protostar, which may indicate that the twist extends to that scale. However the polarisation gradient is likely to be influenced at some level by the asymmetric distribution of dust in the approaching lobe so this might be an over-interpretation of the data.

At $L_B < 15$ AU the field is axial over almost the entire envelope volume, causing the inclination of the point source's polarisation vectors to the disc axis to become smaller. The inclination tends to zero for $L_B \ll R_{cav}$.

In Figure 9(a-c) we illustrate how circular polarimetry would constrain the parameter space. Linear polarimetry is sensitive to the field direction only in along lines of sight where the optical depth is large enough to produce signifi-

cant dichroic extinction. By contrast circular polarisation is produced by dichroic scattering (eg. Gledhill & McCall 2000; Lucas 2003, Whitney & Wolff 2002) and is therefore sensitive to the field direction everywhere in the reflection nebula, provided that there is some grain alignment. Dichroic extinction also influences the circular polarisation state but this complication will not be significant in the optically thin outer parts of the envelope.

Figure 9 illustrates how circular polarimetry has the potential to reveal the scale length of any twist in the magnetic field. Circular polarimetry of HL Tau has been attempted on two occasions using the IRPOL-2 polarimeter at UKIRT. The first attempt during commissioning of the instrument (Takami et al. 1999) indicated that the HL Tau nebula has circular polarisation $\lesssim 1\%$ in the bright central region, though the short exposure time and limited spatial resolution (~ 1 arcsec) would have inhibited detection of higher circular polarisaton further out in the nebula. A second attempt made in 1999 as part of a larger survey (Beckford et al., in prep) suggested that there may be $\sim 2\%$ polarisation in the outflow cavity but the data quality was very

poor so this detection is not secure. A further attempt will be made in better observing conditions.
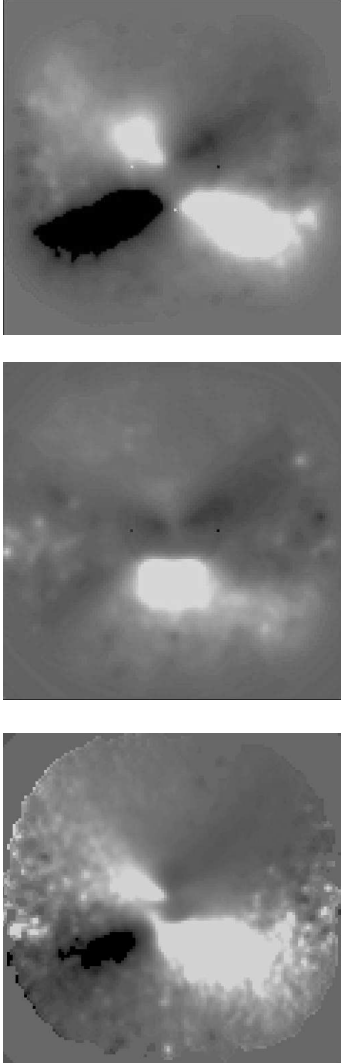

Figure 9. Model circular polarisation maps for HL Tau (Stokes V/I) at K band in 0.4 arcsec seeing. The greyscale ranges from 2% LCP (white) to 2% RCP (black), and the models assume $i = 66°$ and the same physical structure as the successful model described in section 5.2.1. (a) map for an axial field, showing the commonly observed 4-fold or quadrupolar pattern. (b) map for a helical field pitched at $45°$ to the disc axis. (c) map for the pinched and twisted field shown in Figure 8 with $L_B = 100$ AU.

5.2.3   Nature of the dust grains

The dust albedo, the near infrared extinction law and the grain axis ratio were treated as free parameters for the purpose of fitting a successful model to the data. The other optical parameters are (a) the phase function and (b) the 4×4 Stokes matrix and 4×4 extinction matrix which describe the modification of the Stokes vector by scattering and ex-

tinction respectively. For these other parameters a mixture of ralatively small silicate and amorphous carbon grains was used, which produces high linear polarisation at scattering angles near 90° and has a relatively iostropic phase function. However any mixture of small, almost spherical grains would also have the same properties. Small grains in this context means that the scattering cross section of the grain mixture is dominated by grains with size parameter $x < 1$, where $x = 2\pi a/\lambda$, for grain equivalent surface area radius a, and wavelength λ.

Having successfully fitted the data we now examine the implications of the solution for the grain mixture. There are 3 constraints in the successful solution. (1) High linear polarisation is measured in the outer nebulosity in all 3 filters (up to 75% at J band, measuring in 3×3 pixel apertures). Similarly high polarisation has been observed in many YSOs in Taurus, eg. Whitney et al.(1997); LR98, indicating that small grains dominate the scattering cross section in the envelope. To observe such a high polarisation implies that maximum polarisation for single scattering near 90° at J band (P_{Jmax}) must be at least 75%, and probably higher. We conservatively adopt $P_{Jmax} > 75\%$ as the constraint. (2) The extinction law has a ratio of J to K band opacity $\kappa(J/K) = 2.1 \pm 0.31$ (see optical depths in Table 2). This is a shallower extinction law than that observed in the interstellar medium (see below). The H band extinction is fully consistent with this result: $\kappa(J/H) = 1.5 \pm 0.14$ and has smaller uncertainty than the K band value. A shallow extinction is most easily reproduced by an absorptive grain mixture which includes some large grains. (3) The best fit albedo is fairly high: $\omega \gtrsim 0.4$ at H and $\omega \gtrsim 0.2$ at K. This albedo constraint acts in the opposite sense to the linear polarisation: the size parameter of the grains which dominate the extinction cross section cannot be far below unity since the albedo becomes negligible in the small grain limit, unless the grains are perfectly dielectric (zero absorptivity).

Comparison of the output of the Mie scattering code 'bhmie.f of Bohren & Huffman (1989) and the ampld.f code for non-spherical particles demonstrates that the slight oblateness implied by our Monte Carlo fit has a negligible effect on the 3 constraints listed above. We therefore used the bhmie.f code for uniform spheres and the bhcoat.f code for mantled spheres (also from Bohren & Huffman) to search for solutions consistent with the constraints.

Note on extinction law
The near infrared extinction law implied by $\kappa(J/K) = 2.1 \pm 0.31$ is similar to that derived by LR98 ($\kappa(J/K) = 1.8 \pm 0.3$), which was principally determined by modelling of two other low mass YSOs in Taurus, though with qualitative support from additional sources. Recent imaging at very high spatial resolution (Padgett et al.(1999)) has shown that our interpretation of one of these two YSOs, IRAS 04248+2612, was in error. The apparently grey central scattering peak was revealed by Padgett et al. as direct light from a binary protostar, shining through a region of low extinction in the surrounding envelope. In the case of HL Tau it is unlikely that unexpected spatial structure in the foreground affects the derived extinction law. The $\kappa(J/K) = 2.1$ value is largely based on the ratio of polarised flux in the receding lobe to that of the central flux peak. The receding lobe is quite prominent at K band, most prominent at

H band and very faint at J band, a wavelength dependence that cannot be explained by an unexpectedly high or low extinction toward the central source or the receding lobe.

Near infrared extinction in the interstellar medium is observed to be largely independent of the reddening parameter, R_V, almost certainly because interstellar grains are substantially smaller than 1 μm in radius. We note that the opacity ratio for the interstellar medium is variously given as $\kappa(J/K) = 2.52$ (Rieke & Lebofski 1985); $\kappa(J/K) = 2.48$ (Cardelli, Clayton & Mathis 1989, using a $\lambda^{-1.61}$ law); $\kappa(J/K) = 2.69$ (Tokunaga 2000, using a $\lambda^{-1.75}$ law); and $\kappa(J/K) = 2.89$ (Whittet 1992). By contrast previous Monte Carlo modelling by several authors has used opacities based on theoretical interstellar dust models (eg. Mathis, Rumpl & Nordsieck 1977) which are broadly consistent with observations across many wavebands but are not particularly successful in the near infrared. The corresponding opacity ratio of $\kappa(J/K) \approx 3.25$, which we assumed to be correct in LR98, is somewhat larger than the observed values. The difference between the interstellar extinction law and the Taurus extinction law is therefore less than earlier supposed, but is still likely to be real.

Grain mixture solutions

Grain mixtures with an $N(a) \propto a^{-3.5}$ power law and refractive index $n = n' + im'$ were explored with the bhmie.f code and it was found that only mixtures with (a) $m' \sim 0.1$; (b) n' not far in excess of unity; and (c) a size distribution extending to slightly in excess of 1 μm can satisfy the constraints. This region of parameter space is successful because of the Rayleigh-Gans-like optical properties of large grains with a refractive index near unity. The polarisation produced by scattering in the Rayleigh-Gans limit is the same as that produced by Rayleigh scattering (see van der Hulst 1957). The large particles used in successful mixtures are not truly in the Rayleigh-Gans limit ($2x(n' - 1) \ll 1$) but they exhibit similar polarisation properties for sizes up to ($x(n' - 1) \approx 1$), in just the same way as spheres with a larger refractive index have Rayleigh-like polarisation for sizes up to $xn' \approx 1$. Hence large grains with $n' \approx 1$ can have the required combination of small grain characteristics (high polarisation) and large grain characterisitics (shallow extinction law and non-negligible albedo).

A possibly consistent model is that of Pollack (1994) in which small silicate grains are surrounded by thick mantles of water ice, intermingled with more absorptive susbstances. Previous investigation of this model by LR98, using similar observational constraints and the 'dirty ice' optical constants of Preibisch et al.(1993), was not very encouraging. However, the computer code 'refice.f' of Warren (1983) provides a somewhat smaller value of n' for water ice at 10 to 40 K and the extinction law quoted here is slightly less shallow than previously. These two factors make it possible to manufacture grain models consistent with the data. The strong water ice absorption feature observed at 3.05 μm in HL Tau also lends qualitative support to this model (see Figure 10). Water ice is not usually seen in T Tauri stars but is often observed toward more embedded objects such as HL Tau, see Cohen (1975); Kobayashi et al.(1999); Gurtler et al.(1999). Our spectrum is appears consistent with these previous lower resolution data. The hydrogen Pfund series lines may prove useful for quantifying the level of ultraviolet flux in the system, since hydrogen line fluxes at shorter wavelengths are more influenced by extinction and scattering. We therefore provide their equivalent widths: 0.727 ± 0.030 nm for Pfϵ and 0.798 ± 0.050 nm for Pfδ.

The calculated refractive index for pure ice is $n = 1.297 + 1.3 \times 10^{-5}i$ at J band, $n = 1.288 + 2.4 \times 10^{-4}i$ at H band and $n = 1.262 + 2.6 \times 10^{-4}i$ at K band.

In order of increasing sophistication 3 types of model were investigated, the first two of which were successful:

(i) A 1 component model: dirty ice grains with n' as quoted above and $m' = 0.10$ A size distribution with a $N(a) \propto a^{-3.5}$ in the range 0.01 μm $< a < 1.5\mu$m and $N(a) = 0$ otherwise has the following properties. Maximum J band polariastion, $P_{Jmax} = 75\%$; H band albedo, $\omega_H = 0.40$ and opacity ratio $\kappa(J/K) = 2.01$.

(ii) A 2 component model: silicate cores with dirty ice mantles. A core radius of 0.07 μm is adopted, following the interstellar dust model of Li & Greenberg (1997) and the refractive indices from Draine (1985) are used. $m' = 0.11$ was used for the ice mantles, with n' as above. A size distribution $N(a) \propto a^{-3.5}$ in the range 0.07 μm $< a < 1.2\mu$m, where a is the total grain radius and only the mantle has a range of thicknesses, yields the following properties: $P_{Jmax} = 80\%$; $\omega_H = 0.44$; $\kappa(J/K) = 2.14$.

(iii) A 3 component model: silicate cores with dirty ice mantles as above and separate small amorphous carbon grains. Carbon, silicate and water ice are the three most abundant chemical constituents suggested by Pollack (1994). Carbonaceous inclusions would probably also be required to explain the refractive index of the dirty ice. However the observation of Unidentified Infrared Bands (UIR bands) in some YSOs at several wavelengths, including the 3.3 μm wavelength associated with the C-H stretch on aromatic rings, has been widely attributed to very small carbonaceous particles. Such particles were modelled by Preibisch et al.1993, with size distribution $N(a) \propto a^{-3.5}$ in the range 0.005 to 0.03 μm, the upper bound being imposed by various chemical processes (Sorrell 1990). We added amorphous carbon grains to the mixture such that the overall size distribution was $N(a) = Ka^{-3.5}$; $0.005 < a < 0.03$ μm (amomrphous carbon) and $N(a) = Ka^{-3.5}$ 0.07 μm $< a < a_{max}$ (ice mantled silicates), with the same arbitrary constant K being used in both cases. However we found that such a model cannot satisfy the observational constraints for any combination of a_{max} and ice absorptivity $m' = 0.10$, largely because the small absorptive carbon grains reduce the albedo compared with the equivalent model in (ii) above. This suggests that any very small carbon grains must be less numerous than this simple size distribution implies. The absence of 3.3 μm and 3.4 μm UIR band emission in Figure 10 is consistent with this interpretation, though that might be due to insufficient UV flux for excitation of these features.

Finally, we note that alternative grain models with a refractive index near unity could probably be constructed using porous grains in which a significant fraction of the volume is evacuated. A wide variety of grain compositions could then be considered. However the consideration of this far more complicated class of model is beyond the scope of this paper.
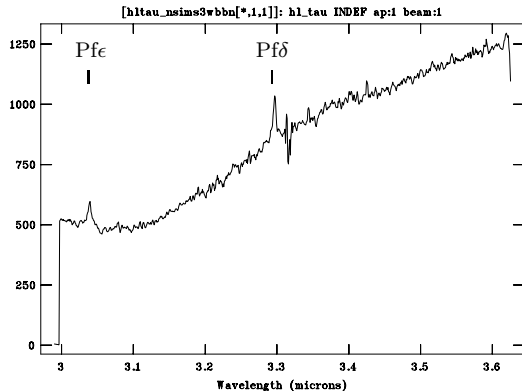
Figure 10. 3-μm spectrum of HL Tau. The water ice absorption band centred at 3.05 μm is quite strong toward this source, providing qualitative support for a model in which water ice dominates the near infrared optical properties of the dust grains. The full extent and depth of the ice absorption is difficult to determine since the continuum rises to longer wavelengths, probably because of continuum emission by hot dust in the inner parts of the accretion disc. Two hydrogen Pfund series emission lines are marked.

6   CONCLUSIONS

High resolution imaging polarimetry of HL Tau with Subaru and UKIRT has produced very similar results from both telescopes. 3-D Monte Carlo modelling of the data with aligned non-spherical grains has allowed us to determine the structure of the circumstellar envelope in considerable detail and has demonstrated that dust in the outflow cavities is required to explain many of the departures from axisymmetry seen in the polarised flux images.

The envelope structure is found to be only slightly flattened, this being tightly constrained by the observations of the receding lobe in the J, H and K bands. An envelope with a radial density profile $\rho \propto R^{-1.5}$ successfully reproduced the data, although slightly shallower profiles are also possible. By contrast the Terebey, Shu & Cassen (1984) density solution for a collapsing and rotating singular isothermal sphere, which has an $\rho \propto R^{-0.5}$ radial density profile in the inner regions and no flattening in the outer regions, did not reproduce the data successfully.

Both lobes of the bipolar outflow cavity contain a substantial optical depth of dust (not just within the cavity walls), and curved, approximately parabolic, cavity walls produce a better fit to the data than conical walls. The small inner accretion disc observed at millimetre wavelengths is not seen at this spatial resolution (0.4 arcsec).

The H and K band polarisation maps show that the polarisation of direct flux from the central point source (the protostar) is inclined by from 32° to 43° to the disc axis. This is s uccessfully modelled with dichroic extinction by aligned grains. At J band the protostar is obscured from view in our data and seen only in scattered light so the polarisation position angle near the protostar is more centrosymmetric. However, the J band polarisation vectors in the vicinity of the protostar show a distortion of the usual centrosymmetric scattering pattern in both magnitude and position angle

which is consistent with dichroic extinction of the scattered light.

Assuming the precession axis of the grains is aligned with the local magnetic field these data can be modelled with a field which is twisted on scales from tens to hundreds of AU, or alternatively by a field which is globally misaligned with the disc axis. A unique solution to the field structure will require sensitive spatially resolved circular polarisation data.

The Monte Carlo models require a near infrared extinction law which is slightly shallower than that observed in the diffuse interstellar medium. Additional constraints on the grain optical properties are very high polarisation in the outer nebulosity and a non-negligible albedo. These optical properties can be fitted using grains with a small refactive index. A possible grain model is composed of silicate cores with dirty water ice mantles in which the largest particles have radii slightly in excess of 1 μm. Such particles have Rayleigh-Gans-like polarisation behaviour, even though they are too large to be truly in the Rayleigh-Gans scattering regime. An alternative grain model with the required small refractive index might be constructed using porous particles, which will be investigated in a future paper.

References

Adams F. C., Shu F. H., Lada C. J., 1988, ApJ, 326, 865

Allen A., Li Z.Y., Shu F.H., 2003, ApJ vol. 599, (in press)

Bacciotti F., Eislöffel J., Ray T.P., 1999, A&A 350, 917

Bastien P., Ménard F., 1988, ApJ 326, 334

Beckwith S., Sargent A. I., Scoville N. Z., Masson C. R., Zuckerman B., Phillips T. G., 1986, ApJ, 309, 755

Beckwith S.V.W., Koresko C.D., Sargent A.I., Weintraub D.A., 1989, ApJ, 343, 393

Beckwith S. V. W., Sargent A. I., Chini R. S., Güsten R., 1990, 99, 924

Beckwith S. V. W. Birk C. C., 1995, ApJ, 449, L59

Bohren C.F., Huffman D.R., 1983, Absorption and Scattering of Light by Small Particles, John Wiley & Sons, New York

Cabrit S., Guilloteau S., André P., Bertout C., Montmerle T., Schuster K., 1996, A&A, 305, 527

Cardelli J.A., Clayton G.C., Mathis J.S., 1989, ApJ, 345,245

Cashwell E.D. Everett C.J., 1959, A practical manual on the Monte Carlo random walk problems (New York: Pergamon)

Close L. M., Roddier F., Northcott M. J., Roddier C., Graves J. E., 1997, ApJ, 478, 766

Cohen M., 1975, MNRAS, 173, 279

Draine B.T., 1995, ApJS, 57, 587

Draine B.T. Weingartner J.C., 1996, ApJ 470, 551

Fischer O., Henning Th., Yorke H.W., 1994, A&A 284, 187

Gledhill T. M., Scarrott S. M., 1989, MNRAS, 236, 139

Gledhill T., Chrysostomou A., Hough J.H., 1996, MNRAS,282,1418

Gledhill T. M., McCall A., 2000, MNRAS, 314, 123

Greene T.P., Lada C.J., 1996, AJ 112, 2184

Gurtler J., Schreyer K., Henning Th., Lemke D., Pfau W., 1999, A&A 346, 205

Hayashi M., Ohashi N., Miyama S. M., 1993, ApJ, 418, L71

Hough J.H., Chrysostomou A.C., Bailey J.A., 1994, Experimental Astronomy, 3, 127

Kobayashi, N., Nagata T., Tamura M., Takeuchi T., Takami, H., Kobayashi Y., Sato S., 1999, ApJ 517, 256

Lazarian, A. 2003, J. Quantitative Spectroscopy & Radiative Transfer 79-80, 881

Li A., Greenberg J.M., 1997, A&A, 323, 566

Lucas P.W., Roche, P.F., 1997, MNRAS 286, 895

Lucas P.W., Roche, P.F., 1998, MNRAS 299, 699

Lucas P.W., Roche P.F., Allard F., & Hauschildt P., 2001, MNRAS 326, 695

Lucas, P.W., 2003, J. Quantitative Spectroscopy & Radiative Transfer 79-80, 921

Luhman K.L., Briceno C., Rieke G.H., Hartmann, Lee, 1998b, ApJ 493, 909

Mathis J.S., Rumpl W., Nordsieck K.H., 1977, ApJ 217, 425

Men'shchikov A. B., Henning Th., 1997, A&A, 318, 879

Men'shchikov A. B., Henning T., Fischer O., 1999, ApJ, 519, 257

Mishchenko M. I., Hovenier J. W., Travis L. D., 2000, Light scattering by nonspherical particles : theory, measurements, and applications, Academic Press, San Diego

Mundt R., Ray T. P., Bührke T., Raga A. C., Solf J., 1990, A&A, 232, 37

Mundy L. G., Looney L. W., Erickson W., Grossman A., Welch W. J., Forster J. R., Wright M. C. H., Plambeck R. L., Lugten J., Thornton D. D., 1996, ApJ, 464, L169

Padgett D.L., Brandner W., Stapelfeldt K.R., Strom S.E., Terebey S., Koerner D., 1999, AJ 117,1490

Pollack, J.B., Hollenbach, D., Beckwith, S., Simonelli, D.P., Roush, T., Fong, W., 1994, ApJ 421, 615

Preibisch Th., Ossenkopf V., Yorke H.W., Henning Th., 1993, A&A, 279, 577

Rieke G. H., Lebofsky M. J., 1985, ApJ, 288, 618

Rodríguez L. F., Cantó J., Torrelles J. M., Gómez J. F., Ho P. T. P., 1992, ApJ, 393, L29

Rodríguez L. F., Cantó J., Torrelles J. M., Gómez J. F., Anglada G., Ho P. T. P., 1994, ApJ, 427, L103

Sargent A. I., Beckwith S. V. W., 1991, ApJ, 382, L31

Shakura N. I., Sunyaev R. A., 1973, A&A, 24, 337

Sorrell W.H., 1990, MNRAS, 243,570

Stapelfeldt K.R., Burrows C.J., Krist J.E., Trauger J.T., Hester J.J., Holtzman J.A., Ballester G.E., Casertano S., Clarke J.T., Crisp D., Evans R.W., Gallagher J.S.III, Griffiths R.E., Hoessel J.G., Mould J.R., Scowen P.A., Watson A.M., Westphal J.A. 1995, ApJ, 449, 888

Takami M., Gledhill T., Clark S., Ménard F., Hough J. H., 1999, Proceedings of Star Formation 1999; ed. T. Nakamoto, Nobeyama Radio Observatory, p. 205-206

Tamura M., Gatley I., Joyce R. R., Ueno M., Suto H., Sekiguchi M., 1991, ApJ 378, 611

Tamura M., Hough J.H., Hayashi S.S., 1995, ApJ, 448, 346

Tamura M., Suto H., Itoh Y., Ebizuka N., Doi Y., Murakawa K., Hayashi S.S., Oasa Y., Takami H., Kaifu N., 2000, Proc. SPIE, 4008, 1153

Tamura, M., Fukagawa, M., Hayashi, M. et al. 2004, in Proc. IAU Symposium 221 "Star Formation at High Angular Resolution" (in press)

Terebey S., Shu F. H., Cassen P., 1984, ApJ, 286, 529

Tokunaga A.T., 2000, in Allen's Astrophysical Quantities; ed. A.Cox, AIP Press, New York

Ulrich R. K., 1976, ApJ, 210, 377

Warren S.G., 1984, Applied Optics, 23, 1206

Weintraub D. A., Kastner J. H., Whitney B. A., 1995, ApJ, 452, L141

Weitenbeck A. J., 1999, AcA, 49, 59

Welch W.J., Hartmann L., Helfer T., Briceño C. 2000, ApJ, 540, 362

Whitney B.A., Hartmann L., 1993, ApJ, 402, 605

Whitney B.A., Kenyon S.J., & Gomèz M., 1997, ApJ,485,703

Whitney B. A. & Wolff M. J., 2002, ApJ, 574, 205

Whittet D.C.B., 1992, Dust in the Galactic Environment, pub IOP, London

Wilner D. J., Ho P. T. P., Rodriguez L. F., 1996, ApJ, 470, L117

Wolf S., Padgett D. L. & Stapelfeldt K. R., 2003, ApJ, 588, 373

Wood K., Reynolds R. J., 1999, ApJ, 525, 799

Yamashita T., Hodapp K.-W., & Moore T. J. T., 1994, ApJ, 422, L21

Yusef-Zadeh F., Morris M., White R. L., 1984, ApJ, 278, 186